

**FACULTY
OF MATHEMATICS
AND PHYSICS**
Charles University

BACHELOR THESIS

Lucia Bajtošová

Distribution of dispersoids in rapidly solidified aluminum alloys

Department of Physics of Materials

Supervisor of the bachelor thesis: doc. RNDr. Miroslav Cieslar, CSc.

Study programme: Physics

Specialization: General Physics

Prague 2019

I declare that I carried out this bachelor thesis independently, and only with the cited sources, literature and other professional sources.

I understand that my work relates to the rights and obligations under the Act No. 121/2000 Coll., the Copyright Act, as amended, in particular the fact that the Charles University has the right to conclude a license agreement on the use of this work as a school work pursuant to Section 60 paragraph 1 of the Copyright Act.

In Prague May 13 2019

signature of the author

I would like to thank the supervisor of my work doc. RNDr. Miroslav Cieslar, CSc. for a guidance through the world of electron microscopy. Moreover, my thanks go to RNDr. Michaela Šlapáková, Ph.D. and Mgr. Jozef Veselý, Ph.D. for their help with SEM and ASTAR software in TEM. Finally, I would like to thank Mrs. Marta Čepová and Ing. Jana Kálalová for their help with a preparation of my samples.

Title: Distribution of dispersoids in rapidly solidified aluminum alloys

Author: Lucia Bajtošová

Department: Department of Physics of Materials

Supervisor: doc. RNDr. Miroslav Cieslar, CSc., Department of Physics of Materials

Abstract: Dispersoids formed during rapid solidification of a quaternary Al-Fe-Mn-Si alloy prepared by twin-roll casting and their transformation after following heat treatment were studied. A conventional transmission electron microscopy and modern automated phase identification methods such as electron backscatter diffraction in scanning electron microscope and automated orientation crystal phase and orientation mapping in transmission microscopy were applied. Energy dispersive X-ray spectroscopy was used to determine the chemical composition of the dispersoids. The phase identification methods were tested on as cast samples and samples annealed for 4 hours at 580 °C. Strategies for statistical evaluation of particle distribution and their crystallographic structure were discussed.

Keywords: Al-Fe-Mn-Si alloy, TEM, EBSD, ASTAR, TRC

Contents

1 Introduction	4
1.1 Phase diagrams and transformations	4
1.1.1 Phase transformations	4
1.1.2 Phase diagram evaluation	4
1.2 Al-Fe-Mn-Si system	4
1.2.1 Ternary subsystems	4
1.2.2 Phases relevant for Al-Fe-Mn-Si system	6
1.3 Introduction to crystallography	7
1.3.1 Electron diffraction.....	7
1.3.2 Miller indices	7
1.3.3 Reciprocal lattice.....	7
1.3.4 Ewald sphere	9
1.3.5 Structure factor	9
1.3.6 Kikuchi line patterns	10
1.4 Experimental techniques	12
1.4.1 Electron diffraction in TEM	12
1.4.2 Camera length	12
1.4.3 Analysis of SAED diffraction patterns.....	13
1.4.4 Electron backscatter diffraction (EBSD).....	13
1.4.5 Energy-dispersive X-ray spectroscopy (EDS)	15
1.4.6 Orientation and phase mapping in TEM (ASTAR).....	15
1.5 Application of experimental techniques	17
1.5.1 EBSD	17
1.5.2 ASTAR.....	17
2 Experimental methods	18
2.1 Examined material.....	18
2.2 Transmission electron microscopy	19
2.3 Scanning electron microscopy.....	19
3 Results and discussion	20
3.1 Phase identification in TEM through SAED patterns	20
3.1.1 As cast state	20
3.1.2 Annealed state	25
3.2 SEM analysis	28

3.2.1 Backscatter-electron imaging	28
3.2.2 EDS analysis	29
3.2.3 EBSD evaluation	31
3.3 ASTAR	34
Conclusions	44
Bibliography	46
List of Figures	50
List of Tables	53
List of Abbreviations	54

Preface

Aluminum alloys exhibit several valuable features such as strength, low density and a good corrosion resistance. They are broadly used in aerospace and automobile industries. Consequently, new demands for further improvement of their mechanical and physical properties appear [1,2]. A crucial role in influencing the strength, hardness, recrystallisation or evolution of texture of the material is played by dispersoids - finely dispersed particles of other phases in aluminum matrix. Their distribution, size and volume fraction depend on a chemical composition and preparation methods of the alloy. Optimization of processing conditions for a further enhancement of materials strength and hardness is currently of a great interest [3,4].

Identification of a crystallographic structure of particles, their orientation and a statistical distribution in the material can help to better understand processes affecting a phase composition of the material and reasons for altered properties observed in this type of material. An analysis of the structure is usually done by transmission electron microscopy (TEM) by an interpretation of diffractograms obtained in a selected-area electron diffraction (SAED) mode. However, this method is laborious and the determination of the statistical distribution of different phases in the material is rather difficult.

Therefore, alternative techniques that can speed up and automatize the identification process were developed. Electron backscatter diffraction (EBSD) combined with energy-dispersive X-ray spectroscopy (EDS) is a relatively well-established technique realized in scanning electron microscope (SEM). Recently, an option allowing the phase evaluation directly in TEM became available - automatic phase and orientation mapping (ASTAR) [5].

The purpose of the present work is to test the potential of the ASTAR automated method for the structure determination and a distribution mapping of phases present in an Al-Fe-Mn-Si based alloy.

1 Introduction

1.1 Phase diagrams and transformations

1.1.1 Phase transformations

Properties of systems composed of two or more chemical substances are significantly different than those of pure substances. Generally, a system consists of several subsystems with essentially uniform physical properties called phases. After a certain time, the system under constant external conditions reaches a thermodynamic equilibrium. Physical properties remain stable and all subsystems are in equilibrium with each other. The modification of external conditions could cause a change of phase composition. To describe the possible coexisting phases and their composition under specified external conditions phase diagrams are used. They provide a useful tool for the analysis of the system behavior despite the fact that in real metallurgical processes equilibrium conditions are usually not reached [6,7].

1.1.2 Phase diagram evaluation

Phase diagrams are constructed either solely through experimental measurements or calculated from thermodynamic data. In thermodynamics, when the temperature and the volume are constant, the equilibrium of the system is reached by minimizing the Helmholtz free energy of the system, and equally, under the constant temperature and pressure the equilibrium is reached by minimizing the Gibbs free energy of the system [6,8].

Therefore, if we are able to evaluate the values of molar free energy of the system for given temperatures, pressures, compositions and structures, then it is possible to determine the phases existing in the equilibrium under these conditions by finding the free energy minimum. Even though obtaining an exact analytical expression describing the behavior of free energy in a multicomponent system is impossible, good results could be received when mathematical models are used [9]. A relatively broadly used thermodynamic modeling method often referred to as Calculation of the Phase Diagram (CALPHAD) simulates the multicomponent phase behavior using the free energy models for individual phases [10].

1.2 Al-Fe-Mn-Si system

Some of the most common additives or impurities in aluminum alloys are Fe, Mn and Si. The mechanical properties of the alloy are influenced by the phases formed in the presence of these elements, therefore, there are repeating efforts to thoroughly investigate the Al rich corner of the quaternary Al-Fe-Mn-Si system.

1.2.1 Ternary subsystems

The Al-Fe-Si, Al-Fe-Mn and Al-Mn-Si are three subsystems relevant for thermodynamic assessment of the quaternary system. Each of them has been

investigated, the relevant phase diagrams were evaluated and compared to the experimental data [11,12].

There are ten stable ternary intermetallic compounds in the Al-Fe-Si system usually denoted by symbols listed in Table 1. The compound with the least amount of Fe and Si are referred to as α and β and they are supposed to be the most stable. The existence and compositions of compounds with higher amount of Fe and Si are not clearly determined because the majority of experimental studies were focused on the Al rich corner (Fig. 1). Also, the recorded compositions of stable phases α and β mentioned in the literature are not uniform probably because of the difference in the material purity and cooling rates [10,13].

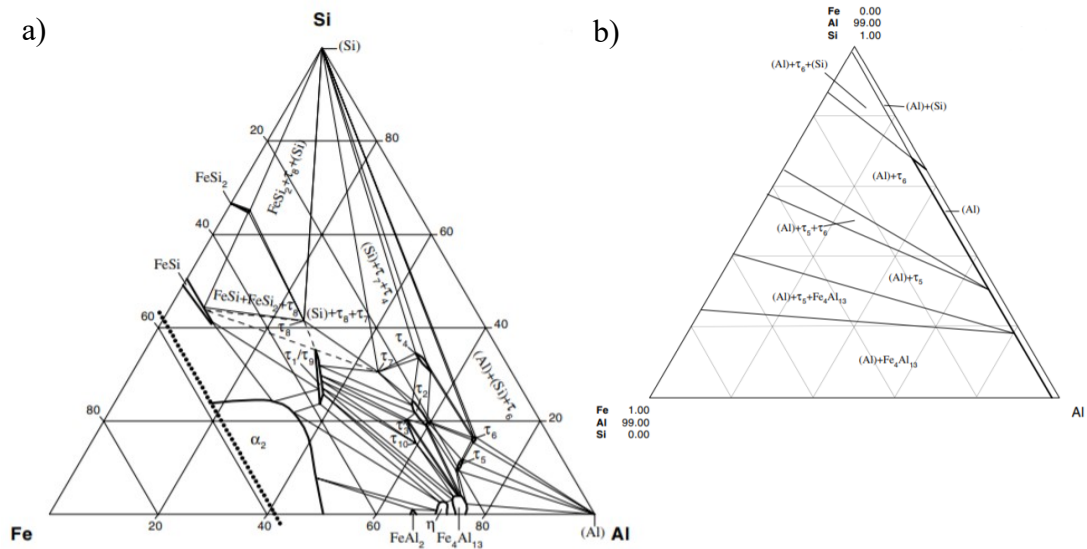


Figure 1: a) Isothermal section of an Al-Fe-Si ternary phase diagram at 550 °C, b) Al-Fe-Si isothermal section of the Al corner at 500 °C [14].

Since the Al-Fe-Mn system plays an important role in both aluminum alloys and lightweight steels, experimental data and thermodynamic evaluations can be found in the literature for both Al rich and Fe rich corners of the system [15]. For our purpose it is sufficient to focus on the Al rich corner (see Table 1).

The Al-Mn-Si system has been a subject of many experimental studies dealing with its thermodynamic properties. A thermodynamic modeling of Al rich corner was also performed, however, the obtained results do not match exactly with experimental data, especially further away from pure Al. Ten ternary phases usually observed in Al-Mn-Si system are listed in Table 1 [16].

Al-Fe-Si		Al-Fe-Mn	Al-Mn-Si	
τ_1	(Al,Si) ₅ Fe ₃	Al ₁₃ Fe ₄	τ_1	Al ₂ Mn ₂ Si ₃
τ_2	(Al,Si) ₇ Fe ₂	Al ₆ Mn	τ_2	Al ₅ Mn ₆ Si ₇
τ_3	Al ₅₅ Fe ₂₅ Si ₂₀	Al ₄ Mn	τ_3	Al ₁ Mn ₁ Si ₁
τ_4	(Al,Si) ₅ Fe ₁	Al ₁₁ Mn ₄	τ_4	Al ₃ Mn ₁ Si ₂
α/τ_5	Al ₇₁ Fe ₁₉ Si ₁₀		τ_5	Al ₃ Mn ₄ Si ₂
β/τ_6	Al ₉ Fe ₂ Si ₂		τ_6	(Al,Mn) ₄ Si ₁
τ_7	(Al,Si) ₃ Fe ₁		τ_8	(Mn, Va) ₆ (Va, Mn) ₂ Al ₁₂ (Al, Si) ₆ (Al, Si) ₂
τ_8	(Al,Si) ₂ Fe ₁		τ_9	Al ₁₄ Mn ₄ (Al, Si) ₅
τ_{10}	Al ₆₀ Fe ₂₅ Si ₁₅		τ_{10}	Al ₂ Mn ₁ Si ₃
τ_{11}	Al ₈₅ Fe ₃₀ Si ₁₅			

Table 1: Phases found in the ternary Al-Fe-Si and Al-Mn-Si systems and Al-rich corner of Al-Fe-Mn system.

1.2.2 Phases relevant for Al-Fe-Mn-Si system

Several assessments of the Al rich corner of the quaternary Al-Fe-Mn-Si system using the experimental data and descriptions of ternary systems were attempted. The experimental investigations confirmed the existence of following ternary phases in the system: α -AlFeSi (Al₈Fe₂Si), β -AlFeSi (Al₅FeSi) and α -AlMnSi (Al₁₅Mn₃Si₂) [17]. The crystal structures of these phases are hexagonal, monoclinic and cubic respectively. Crystallographic characteristics of these phases are listed in Table 2. A considerable solubility of Fe in α -AlMnSi and β -AlMnSi was confirmed [18]. There have been several reports concerning the existence of quaternary phase, however it is also proposed that the α -AlMnSi and β -AlMnSi extend deep within the quaternary system as a result of substitution of Mn atoms by Fe atoms, and no new quaternary phase exists in the Al rich corner of the system. Increase of the Fe ratio leads to the transformation of a simple cubic structure of the α -AlMnSi phase to a body centered structure [18]. The solubility of Mn in compounds of the Al-Fe-Si system is limited and usually neglected in thermodynamic calculations [18,12].

phase	structure	space group	a [Å]	b [Å]	c [Å]
Al ₃ Mn	ortorhombic	P nma	14.883	12.447	12.56
Al ₄ Mn	hexagonal	P63/mmc	19.98		24.673
Al ₆ Mn	ortorhombic	Cmcm	6.4978	7.552	8.870
Al ₃ Fe	hexagonal	6/mmm	5.375		4.374
Al ₁₃ Fe ₄	monoclinic	C2/m	15.488	8.086	12.477
Al ₅ FeSi/ β/τ_6	monoclinic		6.161	6.175	20.813
Al ₈ Fe ₂ Si/ α/τ_5	hexagonal	P63/mmc	12.404		26.23
α -AlMnSi	cubic	Pm3	12.68		
β -AlMnSi	hexagonal	P63/mmc	7.153		7.754

Table 2: The confirmed phases found in the Al-Fe-Mn-Si system with their crystallographic structures and lattice parameters [19-22].

1.3 Introduction to crystallography

1.3.1 Electron diffraction

Accelerated electrons could be elastically scattered on crystal lattices because of their short wavelength. An analysis of diffraction patterns enables to obtain several crystallographic information about the material. When working with a thin specimen, good qualitative results can be obtained using a kinematic theory of electron diffraction.

Let there be a primitive crystal lattice with a set of parallel planes with interplanar distance of d (Fig. 2). When an electron beam enters the lattice, electrons are scattered on individual equidistant lattice atoms. Because the secondary diffraction is neglected due to the first-order Born approximation in the kinematic theory, a positive interference occurs when a condition

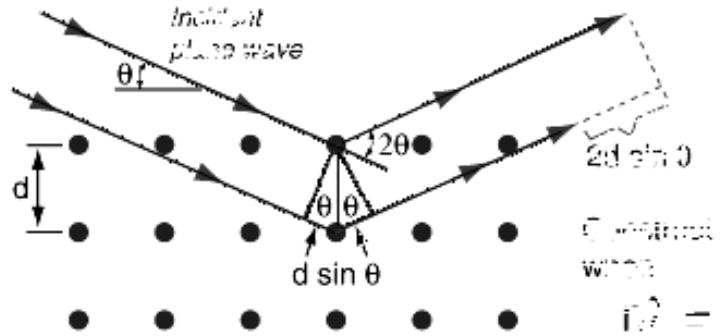


Figure 2: Positive interference of an electron beam scattered on a crystal lattice with interplanar distance of d [25].

$$2d \sin \theta = n \lambda \quad (1)$$

is satisfied, where θ stands for an angle of the incident beam and the crystal lattice as drawn in Fig. 2. Therefore, beam of electrons with a fixed wavelength λ interacting with a set of planes of spacing d is diffracted with a strong intensity only if it propagates under a certain angle θ_B called the Bragg angle [23].

Because of a short wavelength of accelerated electrons compared to the lattice spacing, Bragg angle is very small, and strong diffractions are realized only on planes almost parallel to the direction of the incident electron beam [24].

1.3.2 Miller indices

A system of planes in a crystal lattice is generally denoted by three integers inside parentheses (hkl). The values of these integers for each plane are given by inverse of the points where a plane intercepts the base vectors. The result is subsequently multiplied by the lowest common denominator so that relatively prime integers remain [25].

1.3.3 Reciprocal lattice

Electron number density in a crystal lattice is a periodic function of a distance in each of three lattice axes. After expanding of this function into an exponential form of

Fourier series, the allowed vectors for which this series remains invariant under all crystal translations determine the reciprocal lattice vectors.

For that reason, the primitive reciprocal lattice base vectors \mathbf{b}_1 , \mathbf{b}_2 , \mathbf{b}_3 are constructed as:

$$\mathbf{b}_1 = 2\pi \frac{\mathbf{a}_2 \times \mathbf{a}_3}{\mathbf{a}_1 \cdot \mathbf{a}_2 \times \mathbf{a}_3}, \quad (2)$$

where \mathbf{a}_1 , \mathbf{a}_2 , \mathbf{a}_3 are primitive base vectors of the direct lattice. The factor 2π is usually not used by crystallographers [26].

As follows from the definition, \mathbf{b}_1 , \mathbf{b}_2 , \mathbf{b}_3 satisfy the condition

$$b_i a_j = \delta_{ij}, \quad (3)$$

where δ_{ij} stands for Kronecker delta.

Each vector of the reciprocal lattice \mathbf{g} can be expressed in a form

$$\mathbf{g} = \nu_1 \mathbf{b}_1 + \nu_2 \mathbf{b}_2 + \nu_3 \mathbf{b}_3, \quad (4)$$

where ν_1 , ν_2 , ν_3 are the corresponding scalar coefficients.

Following properties of the reciprocal vector can be derived from (3):

The reciprocal lattice vector is perpendicular to a plane with Miller indices corresponding with the vector components.

The length of the vector corresponding to a certain system of planes is equal to the inverse value of their interplanar distance.

$$|\mathbf{g}_{hkl}| = 1/d_{hkl}. \quad (5)$$

Examination of the relation between the reciprocal vector and diffraction conditions in a crystal lattice shows that the strongest diffraction occurs when the scattering vector of diffracted wave is a vector of the reciprocal lattice

$$\Delta \mathbf{k} = \mathbf{g}, \quad (6)$$

where the scattering vector $\Delta \mathbf{k}$ is defined as a difference between wave vectors of the incident beam and the scattered beam [23,25].

1.3.4 Ewald sphere

The relationship between the scattering vector and the reciprocal lattice vector can be geometrically represented by an Ewald construction (Fig. 3). Vector $-\mathbf{k}$ is constructed at the origin of the reciprocal lattice representing the crystal. With the terminal point of the vector $-\mathbf{k}$ as a center, a sphere with radius $1/\lambda$ is drawn. Since the wavelength of the scattered wave is the same as that of the initial one during elastic scattering, the surface of the sphere can be interpreted as a set of all possible wave vectors of the waves elastically scattered on the crystal lattice. Then the diffraction condition (6) is equal to the statement that the diffraction occurs when the surface of the Ewald sphere intersects a reciprocal lattice point [24].

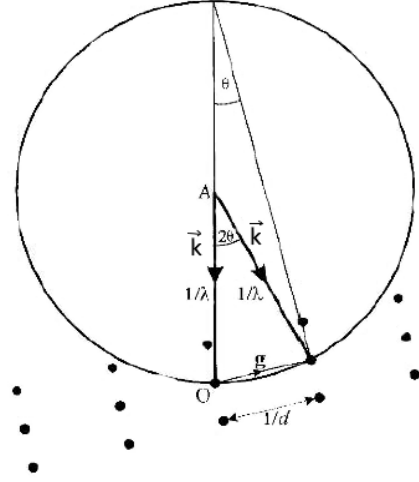


Figure 3: Ewald construction [23].

In the case of accelerated electrons, the radius of the Ewald sphere ($\sim 10^{12} \text{ m}^{-1}$) is considerably larger than the plane spacing of the reciprocal lattice ($\sim 10^{10} \text{ m}^{-1}$). Therefore, the sphere can be approximated as a plane near the origin of the reciprocal space and the diffraction pattern is equivalent to a projection of the reciprocal plane containing the origin of the reciprocal lattice, which is perpendicular to the initial wave vector \mathbf{k} .

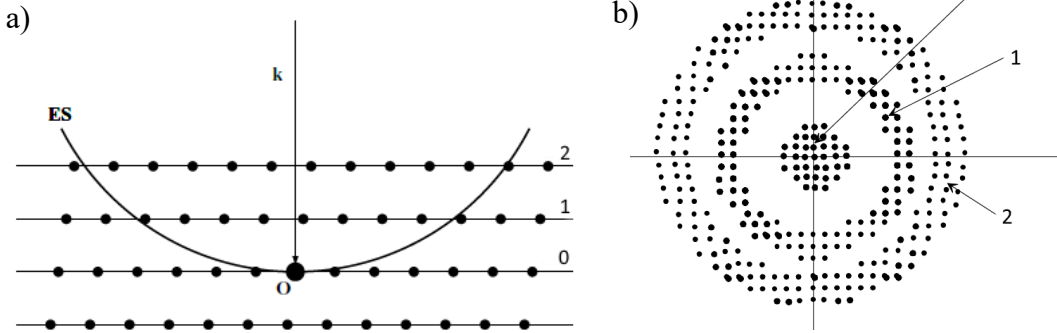


Figure 4: Formation of high order Laue zones. a) Ewald sphere intersecting several parallel reciprocal lattice planes, b) corresponding diffraction pattern [27].

However, the curvature of the Ewald sphere is not fully neglectable. Diffraction spots from planes parallel to the plane containing the origin can appear in the diffractogram at higher diffraction angles (Fig. 4). They are referred to as high order Laue zones [28].

1.3.5 Structure factor

The intensity of an electron beam diffracted on a crystal lattice varies for different diffraction planes. Using the kinematical diffraction theory, it can be shown that it is proportional to the intensity of the initial beam and the structure factor F_{hkl}

$$F_{hkl} = \sum_{j=1}^n f_j \exp[-2\pi i(hu_j + kv_j + lw_j)], \quad (7)$$

where (hkl) are the Miller indices of the corresponding diffraction plane, u_j, v_j, w_j indicate the coordinates of the atoms in the lattice unit cell and f_j refers to the atomic scattering factor, a constant value distinct for individual atom types. Since the crystal lattice is of a periodic character, it is sufficient to calculate the structure factor for a sole unit cell. The correlation between the intensity of the diffracted beam and the structure factor causes the disappearance of so-called forbidden diffraction spots [25,28].

1.3.6 Kikuchi line patterns

If a diffraction pattern is taken from a thicker area of a crystal, several lines appear along with diffraction spots. These lines, generally known as Kikuchi lines [23], form patterns characteristic for each crystal structure and orientation. Their appearance is a result of inelastically scattered electrons subsequently elastically scattered on two parallel crystal planes.

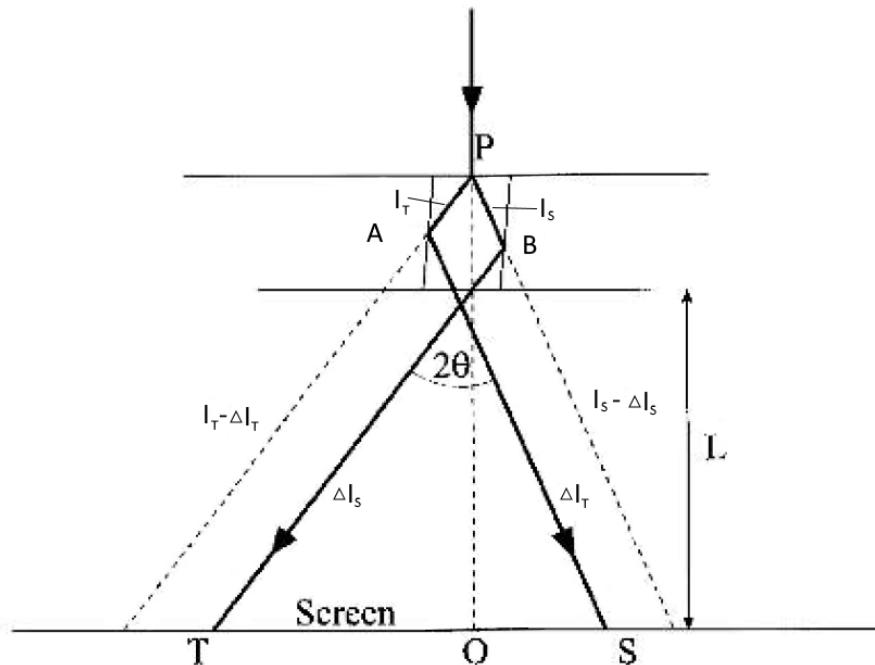


Figure 5: Formation of a Kikuchi lines [28].

As drawn in the Fig. 5, electrons inelastically scattered at a point P propagate in all directions with an intensity proportional to the direction of the original non-scattered beam. Arriving at the parallel planes at the Bragg angle the electrons diffract and change the direction of their propagation in accordance with the Bragg's law. Notice that electrons

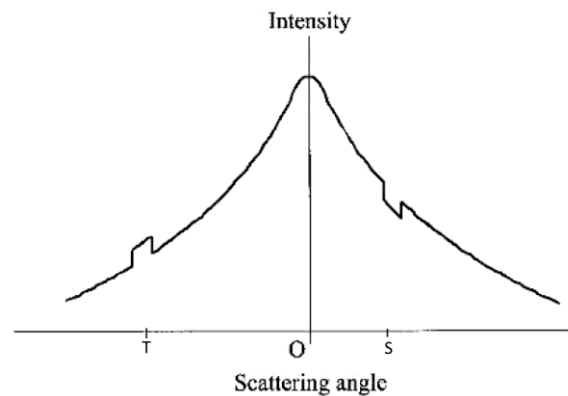


Figure 6: The intensity of inelastically electron scattering resulting in a formation of a Kikuchi line pattern [28].

diffracted on the plane A propagate closer to the direction of the original beam therefore their intensity is larger than the intensity of those diffracted on the plane B. Now consider point T. The overall intensity arriving to this point is due to the diffraction $I_T + \Delta I_S - \Delta I_T > I_T$ so the final intensity is larger than when the Bragg diffraction does not occur. Similarly, the overall intensity in the point S equals $I_S + \Delta I_T - \Delta I_S < I_S$ (Fig. 6).

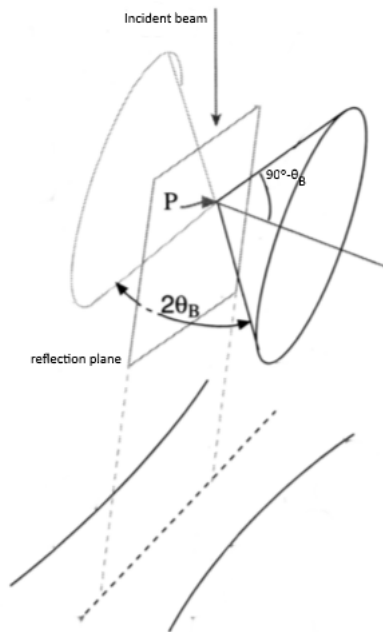


Figure 7: Formation of Kikuchi lines in a three-dimensional space [24].

In three dimensions, the scattered electrons form two conical surfaces whose intersection with the Ewald sphere results in two hyperbolas with a distinctive intensity (Fig. 7). As mentioned above, the radius of Ewald sphere for accelerated electrons is very large, hence the hyperbolas appear as straight lines on a small screen of the microscope. Kikuchi lines are connected to a certain system of planes and unlike the diffraction spots they move when the specimen is tilted, enabling thus to find an exact crystal orientation [24,28].

1.4 Experimental techniques

1.4.1 Electron diffraction in TEM

The most common way to obtain electron diffraction patterns is through transmission electron microscope. All parallel beams leaving the specimen pass through the objective lens and intersect in one point of back focal plane of the lens (Fig. 8). Focusing the optical system behind the objective lens on the back focal plane enables an observation of the diffraction pattern of the specimen. To form a SAED pattern a diffraction aperture is used to select only a small area of the specimen [23].

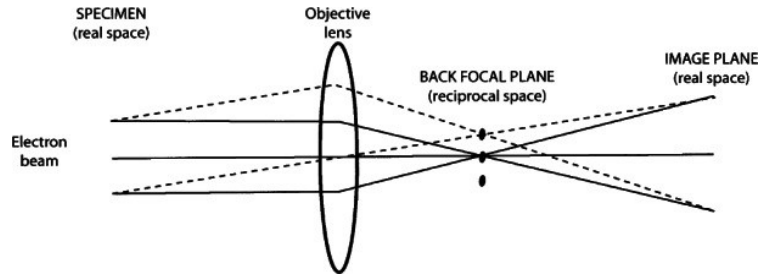


Figure 8: The difference between a diffraction image observation mode and an image observation mode in TEM [29].

1.4.2 Camera length

Distance between diffraction spots in diffraction patterns is directly proportional to the camera length, which is defined as a distance between the sample and the projected image where the camera is placed [30].

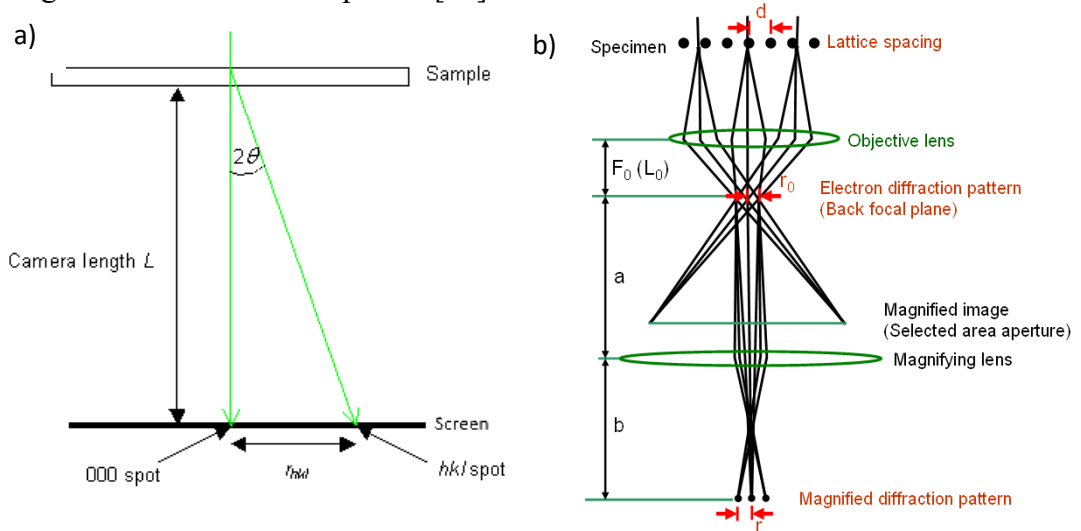


Figure 9: a) Camera length, b) effective camera length in TEM.

Under a low angle approximation $\sin \theta \approx \theta \approx \tan \theta$ a relation between camera length L , wavelength λ , diffraction spot distance r_{hkl} , interplanar distance d_{hkl} related to a system of planes (hkl)

$$r_{hkl}d_{hkl}=\lambda L \quad (8)$$

can be derived from the Bragg's law [31] and a geometry of the Figure 9a [30].

If lenses are used to change the direction of the electron beam, the original diffraction spots distance is altered, and it is necessary to use an effective camera length. After placing an objective lens between the specimen and the projected image, the new effective camera length is equal to the focal length of the lens. Further magnification of the image by other magnifying lens modifies the new effective camera length by a factor b/a where b stands for the distance between the lens and the magnified image and a is the distance between original diffraction pattern and the lens (Fig. 9b) [32].

In a real microscope, it is necessary to calibrate the camera length on a sample with a known lattice constant [30].

1.4.3 Analysis of SAED diffraction patterns

When the SAED aperture is used, the diffraction pattern is formed only by a diffraction of electrons on a limited volume of the crystal. If possible, the most advantageous is to obtain a diffractogram from a single crystal with one crystallographic orientation. In this case, the diffraction pattern consists only of regularly placed spots.

Taking the diffraction pattern as a projection of a reciprocal lattice perpendicular to the incident beam, it becomes evident that the distance between the center of the diffractogram and one of the diffraction spots is equal to the reciprocal vector corresponding to a system of planes where the Bragg condition is satisfied [24,28].

If the crystal structure is known, the indexing of the diffraction spots could be easily done by comparing sections of the reciprocal lattice with the acquired diffraction pattern. If the structure is unknown, it is necessary to obtain at least two diffractograms and find similarities in several most probable structures. Only after confirming the identity of both diffractograms with two sections of the reciprocal lattice and equality of the angle measured between the tilts of the sample, at which the diffractograms had been obtained, with the angle of the corresponding sections, the predicted structure is validated with a high probability.

1.4.4 Electron backscatter diffraction (EBSD)

Electron backscatter diffraction is an experimental technique performed in a scanning electron microscope used for a determination of the crystal structure and the orientation of a chosen surface area. Grain boundary types and misorientations can be also monitored.

The surface of the sample is scanned by a focused probe of electrons (Fig 10a) They change their trajectory because of the interaction with the Coulomb field of the atoms. After several interactions a part of electrons called backscattered electrons emerges back from the specimen. During their propagation in the sample the scattered electrons diffract on a system of crystallographic planes and form two conical surfaces. As a result, the electron backscatter diffraction pattern takes form of Kikuchi bands analogous to the ones formed in TEM. Their relation to the lattice planes of the crystal allows to obtain information about the crystal structure and orientation (Fig 10b) [33].

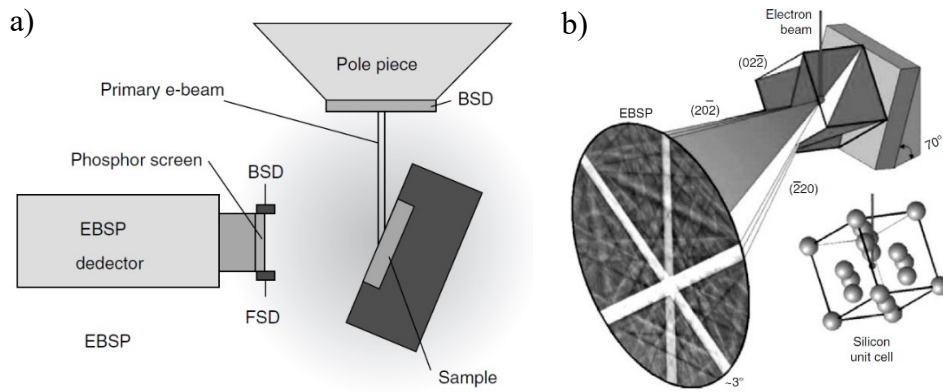


Figure 10: a) Arrangement of a sample and an electron beam scattering pattern (EBSP) detector with backscatter and forescatter electron detector diodes (BSD) and (FSD) in SEM, b) electron interaction with crystalline material [33].

Corresponding electron backscatter diffraction patterns are point by point collected by a camera from a phosphor screen. To increase the number of scattered electrons, the sample is usually tilted approximately 70 degrees in respect to the electron beam [34,35].

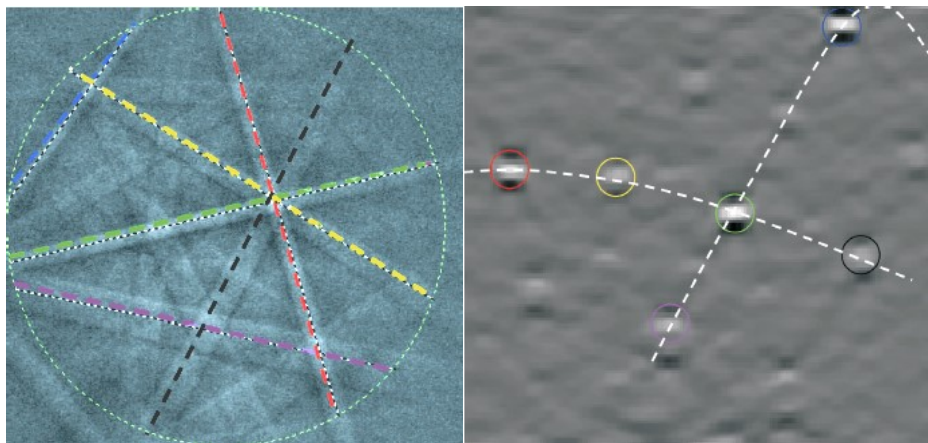


Figure 11: Transformation of Kikuchi lines from a screen into points in a Hough space [36].

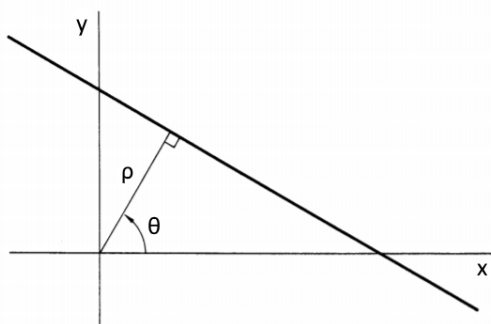


Figure 12: Parameters of the Hough space [37].

For the purpose of a simpler determination of crystal orientations, the Kikuchi lines are converted into single points in the Hough space (Fig. 11). The Hough transform of a straight line (Fig. 12) is given by an expression

$$\rho = x \cos(\theta) + y \sin(\theta) \quad (8)$$

The parameter space with the parameters θ, ρ is equivalent to Hough space [37].

However, certain restrictions concerning the range of use of this method exist. The distinctness of Kikuchi lines is related to the structural damage and contaminations of the sample surface, therefore well-polished samples are necessary. Moreover, the Kikuchi lines can be affected by a plastic deformation state of the crystallite. Increasing strain and internal stresses can lead to their disappearance [35].

1.4.5 Energy-dispersive X-ray spectroscopy (EDS)

A high-energy electron beam is directed on the surface of the sample where it interacts with atoms. According to a quantum theory, each atom is composed of a nucleus surrounded by electrons occupying set of discrete quantum states with different energy levels called atomic orbitals [38]. Values of allowed energies are unique for each element. When an electron is released from one of the low energy atomic orbitals, spontaneous emission occurs when an electron from a higher energy state fills its place while emitting an X-ray photon of energy equal to the difference of the energy of the two considered quantum states. Since one of the possible beam-sample interactions involves an ejection of an electron from the low energy atomic orbital, a unique set of X-rays characteristic for each element can be detected. Interaction of an X-ray with

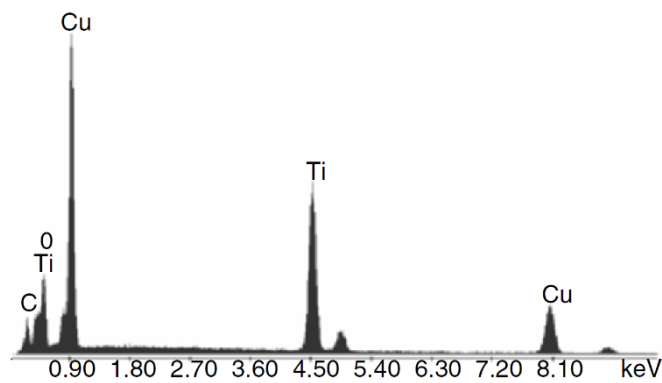


Figure 13: EDS spectrum for TiO₂ particles on a Cu substrate [33].

the EDS detector causes a formation of a charge pulse proportional to the X-ray energy. The pulse is afterwards converted to a voltage pulse, its energy is determined and saved. The elemental composition of the sample can be calculated from the number of pulses with the same energy in the EDS spectrum (Fig. 13) [28,39].

1.4.6 Orientation and phase mapping in TEM (ASTAR)

In order to avoid difficulties linked to the use of the EBSD described above it is possible to complete orientation mapping in TEM. The beam is scanned over the sample and electron diffraction patterns from different spots of the scanned area are collected. Experimentally obtained diffraction spot patterns are subsequently compared to pre-calculated templates and orientation of the crystal is computed [40,41].

Far better reliability of this technique can be achieved by precession of the primary electron beam around the optical axis of the microscope (Fig. 14). Intensities of rotating beam diffraction spots are a result of an integration of diffraction intensities over a range of angles satisfying the Bragg condition. This leads to the reduction of dynamical effects of the electron diffraction. Kinematically forbidden reflections in the non-precession electron diffractogram appearing sometimes as a result of multiple diffraction are also suppressed [25]. While using the same scanning step sizes the crystal orientation map derived from the precession electron diffraction spot patterns was shown to be more accurate than the map obtained with a non-precessing beam [41,43].

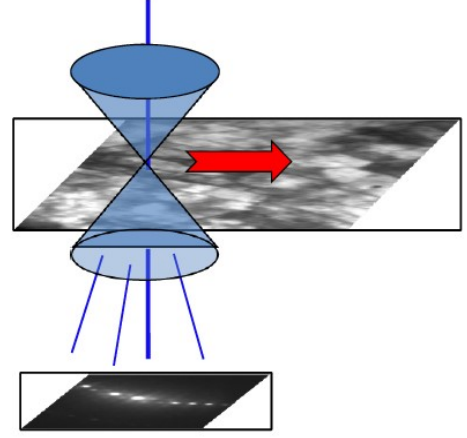


Figure 14: Scanning direction of the precession beam over the sample [42].

The sample is represented as a thin film for the calculation of templates and only the kinematical diffraction theory is used to receive computed diffraction patterns. In the template, each reflexion is characterized by a triplet composed of the spot position (x and y) and its intensity. To determine the best match between the calculated template and the experimental electron diffraction spot patterns, correlation index defined as

$$Q_i = \frac{\sum_{j=1}^n P(x_j, y_j) T_i(x_j, y_j)}{\sqrt{\sum_{j=1}^n P^2(x_j, y_j)} \sqrt{\sum_{j=1}^n T_i^2(x_j, y_j)}} \quad (9)$$

is used. In this equation, the diffraction pattern is represented by the intensity function $P(x, y)$ and every template is given by the function $T_i(x, y)$. Note that each template contains only few tens of non-zero points whatever the size of the picture. Higher correlation index indicates better match of the experimental diffraction pattern and the pre-calculated template [44].

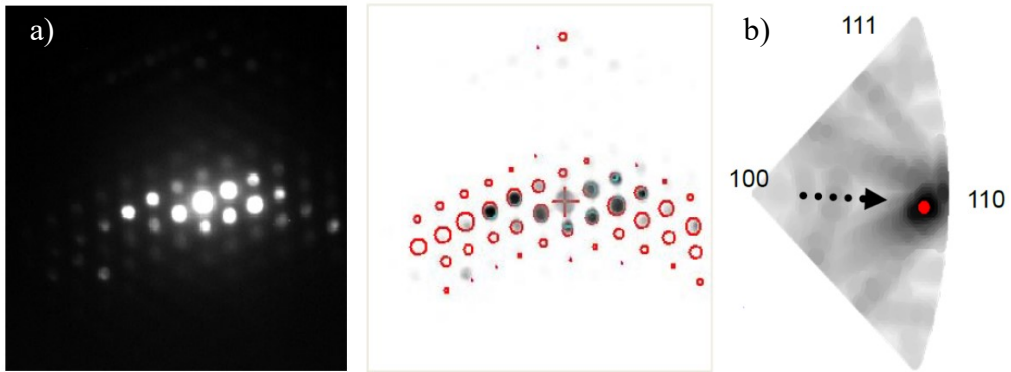


Figure 15: a) Matching of the obtained diffraction patterns and pre-calculated templates represented by red circles. b) Orientation triangle showing the most probable orientation [42].

After plotting calculated correlation indices to a standard stereographic triangle where a darker color implies a higher correlation index, the most probable crystal orientation emerges (Fig. 15).

Scanning step size can be adjusted according to needs. The smallest step can go down to 1 nm and delivers much higher spatial resolution than the one obtained by SEM EBSD method.

1.5 Application of experimental techniques

Above described experimental techniques have already been tested and used on a variety of samples of different materials by a wide range of researchers. A review of already conducted experiments follows.

1.5.1 EBSD

The roots of EBSD lie almost one century in the past, when the first electron back-scatter diffraction pattern was observed by Japanese physicist Seishi Kikuchi [45]. Only after development of an automated orientation determination around two decades ago did the technique gain recognition and became one of the most utilized methods for microstructural analyses of crystalline materials. Since then, it has been improved, perfected and it handles many areas of applications including evaluation of texture, strain gradient, grain morphology and boundaries or identification of phases and material defects on various materials such as metals, alloys, minerals, ceramics and semiconductors [35].

In this work, the method has been applied on Al-Fe-Mn-Si alloys for the purpose of orientation and phase distribution mapping. Similar work on Al-Fe-Mn-Si alloys with a different composition was already realized by Lukáš [37]. A combination of EBSD and EDS methods lead to a successful identification of α -AlMnSi cubic phase, Al₈Fe₂Si hexagonal phase and Al₆Mn phase in the cold rolled and subsequently annealed at 450 °C AW-3003 and AW-8006 alloys. The orientation of the grains has also been determined [37].

More successful phase evaluations have been performed on Al-Fe-Si and multicomponent Al-Si based alloys [46-48]. Certain problems frequently arise with attempts of orientation identifications of α -Al(Fe,Mn)Si cubic phase. This problem has been reviewed by Becker in [48] who ascribes the occurrence of five strongly scattered different orientation solutions to the pseudosymmetry of the α -Al(Fe,Mn)Si crystal structure. One way to obtain the correct solution is a manual band detection which, however, strongly lowers the advantages related to the quickness of the EBSD technique. Another method which increases the frequency of the correct solution while applying standard indexing is an increase of the Hough-space resolution.

1.5.2 ASTAR

The automated orientation crystal phase and orientation mapping was developed only recently [49] and only its upgrade by using precession electron diffraction few years later [50] allowed the acquisition of accurate data. The new method has been tested mainly on austenitic steels, later on a polycrystalline copper and MnAs rich crystallites

in GaAs matrix. After a commercialization of the technique by a company NanoMEGAS, it has slowly gained more popularity and it continues to be tested on a larger scale of different materials. However, compared to well established EBSD method, the reports of a successful exploitation of ASTAR are scarce.

An orientation investigation has been performed on Al-Cu-Mg alloy in which equilibrium precipitates θ -Al₂Cu and S-Al₂CuMg were present. θ -Al₂Cu is a body-centered tetragonal structure with lattice parameters $a = 6,603 \text{ \AA}$ and $c = 4,872 \text{ \AA}$, S-Al₂CuMg is base-centered orthorhombic with lattice parameters $a = 4,010 \text{ \AA}$, $b = 9,250 \text{ \AA}$ and $c = 7,150 \text{ \AA}$ [51]. The phase distribution and grain orientation has been satisfactorily mapped by ASTAR without any indexing difficulties [52].

Complications concerning the indexing of the diffraction patterns were encountered by Ghamarian while studying microstructure of ultrasonically treated Ti-6Al-4V when faint diffraction spots appeared behind the main diffraction pattern [53]. The occurrence of overlapping patterns is frequent in samples where the grain size is considerably smaller than the thickness of the foil. In this case, it is more suitable to use the EBSD technique. The second, less probable reason for such an occurrence could be lattice distortions and degradation of diffraction patterns caused by severe plastic deformation. Since no plastic deformation methods were applied on samples in this work, this reason does not need to be considered.

2 Experimental methods

2.1 Examined material

The studied materials were prepared by a company AIB Břidličná, a. s. The studies were conducted on Al-Mn-Fe-Si alloy with a following composition of the main alloying constituents:

Al	Fe	Mn	Si	Ti
balance	0.350	0.002	0.369	0.019

Table 3: Composition of the AA1200 alloy in wt. %.

A small amount of Ti added in the material does not affect the phase composition and only acts as a grain refiner and an antirecrystallizing agent.

The material was prepared by a twin-roll casting in which the molten metal is poured between two water cooled rolls where it concurrently solidifies and is rolled to the strip of thickness 8 mm. A selected part of the samples was annealed for 4 hours at 580 °C enabling a full recrystallization of a strip. Both as cast and annealed samples were analyzed.

2.2 Transmission electron microscopy

Specimen for TEM were cut by a diamond saw from the original strip. 0.15 mm thin plates were prepared by a mechanical grinding machine Struers Dap -7. Circular discs of diameter 3 mm were mechanically punched out of the plate. After that, the discs were electrolytically etched at TenuPol-5 by 30 vol.% nitridic acid in methanol at -20 °C for around one minute, the time sufficient for a formation of a small hole surrounded by an extremely thin material area suitable for the observation in TEM.

Transmission electron microscope JEOL JEM 2000FX with 200 kV accelerating voltage was used during observations. For this purpose, the samples were placed in a double tilt analytical holder and the diffraction pattern was captured by an in-built camera Veleta in a diffraction mode. The pictures of analyzed particles were acquired in a bright field mode.

Precession electron diffraction patterns were obtained and automatically matched to the predefined phases at TEM JEOL 2200FS operated at 200 kV, equipped with “Spinning Star” electron precession from NanoMEGAS with an ASTAR software package.

2.3 Scanning electron microscopy

The samples for SEM were grinded on SiC papers and polished on a rotating disc with a diamond suspension. One of the samples was afterwards electrolytically polished by 30% nitridic acid in methanol for 10 s in Struers LectroPol-5.

The microscope FEI Quanta FEG 200 was used for observations. The surface morphology of the samples was obtained by detecting the secondary electrons. EDAX EDS system was used to define the elements present in the examined phases. EBSD was used to map the phase distribution in materials.

3 Results and discussion

3.1 Phase identification in TEM through SAED patterns

The first step in the evaluation of the dispersoid distribution in the studied material is the determination of the crystallographic structure of phases present in the material, which is a valuable impact information for a further evaluation with automated techniques. This is done on SAED pattern obtained from a range of dispersoids found in the material as explained in the introduction. Since only the phases listed in Table 2 are expected, received diffractograms are firstly related and indexed with accordance to those structures.

Experimental patterns are compared with theoretical diffraction patterns simulated by a program JEMS [54]. The program uses the already known atom positions in a unit cell of the corresponding phase. The distances of the diffraction spots from the center are measured along with angles between spots located close to the primary beam. When the accordance between measured and calculated distances is found, the simulated diffraction patterns for possible orientations are reviewed until all the distances and angles are identical and the match is found within an experimental error. Indexing highly symmetrical diffraction patterns with a short distance between diffraction spots is less complicated since the patterns belong to the crystal orientations with small values of Miller indices. If a match between an experimental and simulated diffraction pattern could not be found, it is usually because the diffraction pattern from an orientation with a high value of Miller indices was captured. In this case, it is often necessary to gather more experimental data.

3.1.1 As cast state

TEM observations in the bright field mode reveal that mostly ellipsoidal but also randomly shaped rounded dispersoid particles with the size from 1 μm to 2 μm forming clusters can be found in the aluminum matrix (Fig. 16). Compared to the pictures of most probable phases found in the literature, observed shapes resemble the cubic α -Al(Fe,Mn)Si phase [48,55] or some of the coarser ones the hexagonal Al₄Mn phase [56]. β -Al(Fe,Mn)Si phase usually forms thinner needle-like particles than the ones detected in our material [55]. To confirm the assumptions based on the particle shape, the analysis of diffraction patterns captured in diffraction mode is necessary.

For the purpose of getting a clear unambiguous diffraction pattern, particles in a very thin area of the sample near the edge of the hole were chosen.

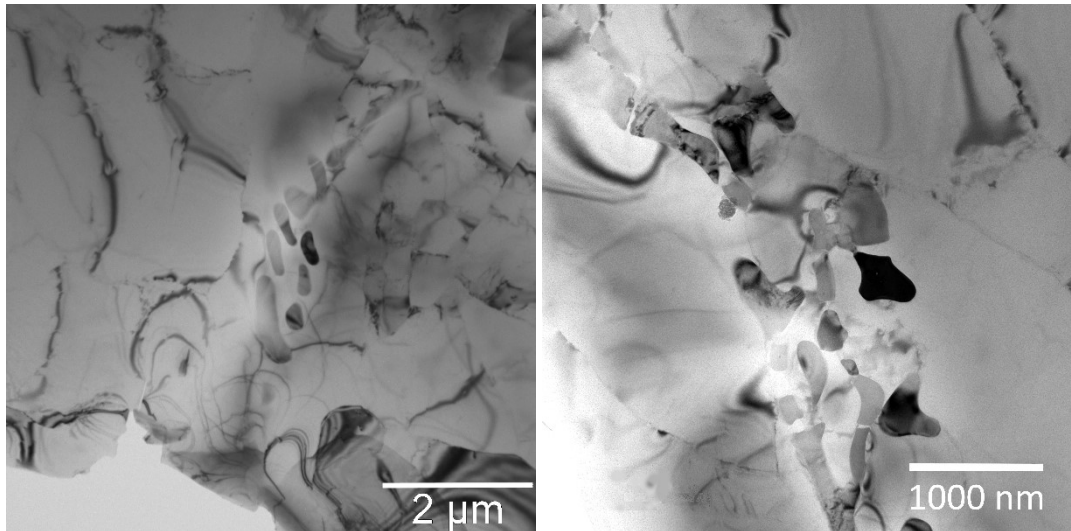


Figure 16: Bright field images of the as cast AA1200 sample.

Diffraction patterns of several different particles were acquired and evaluated. The BF image of particles and their corresponding diffractograms are shown in Figures 17-20.

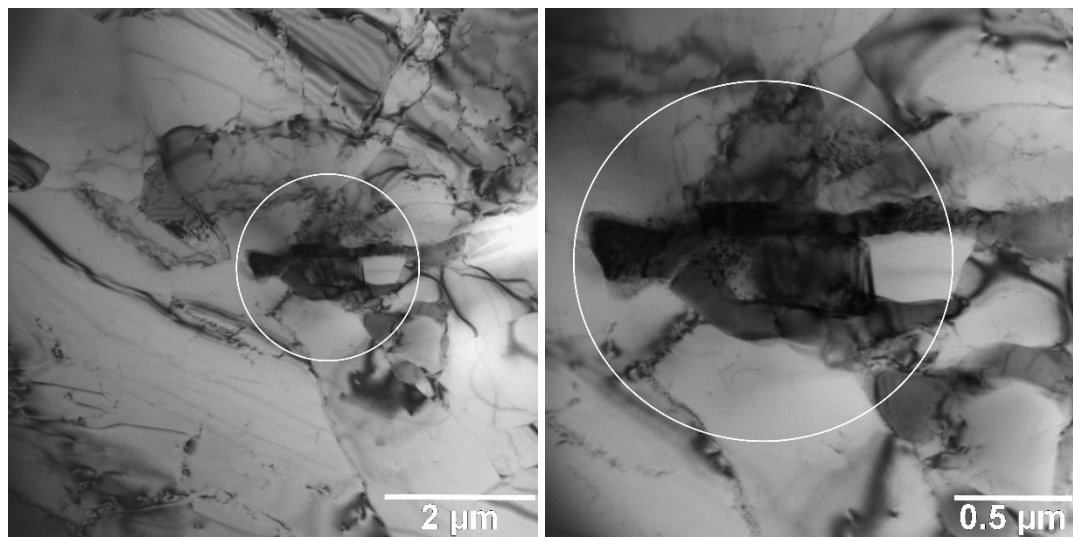


Figure 17. BF image of a dispersoid particle A used for phase identification.

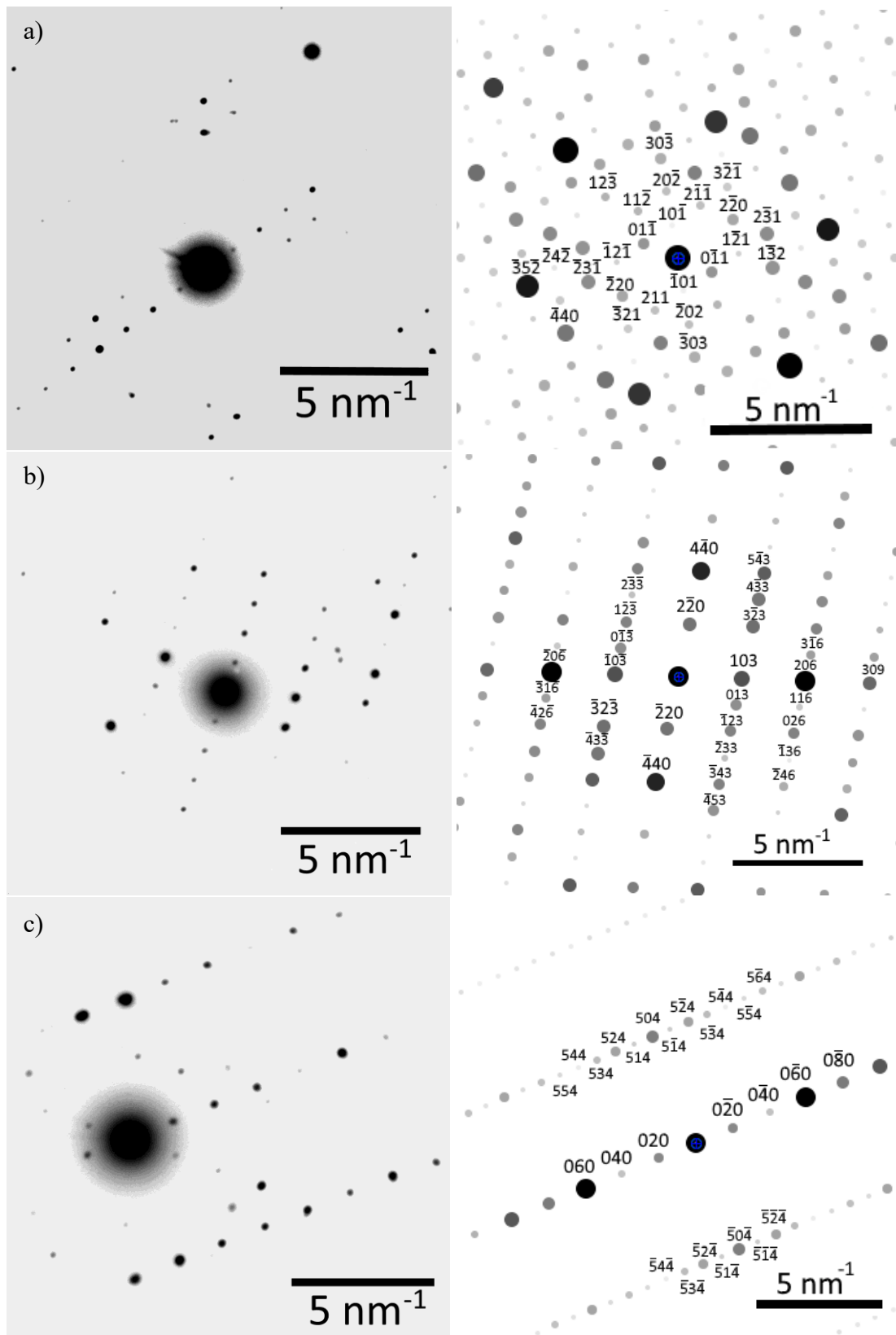


Figure 18: Diffraction patterns obtained from particle A and their corresponding simulated diffraction patterns of Al_3Mn phase with following normal vectors: a) $[1\ 1\ 1]$, b) $[3\ 3\ \bar{1}]$, c) $[\bar{4}\ 0\ 5]$.

The diffraction pattern in Fig. 18a corresponding to the particle A appears as a pattern of regular equilateral triangles with side length 1.12 nm^{-1} and angles 60° characteristic for a cubic $\alpha\text{-Al(Fe,Mn)Si}$ phase. However, after a closer examination a small difference between the side lengths can be discovered implying that the triangles are isosceles with side lengths of 1.12 nm^{-1} and 1.04 nm^{-1} . Measurement of all the angles confirmed a non-equilaterality of the triangle with their actual values being around 57° and 65° . The diffractogram was identified as an orthorhombic Al_3Mn phase near the crystal orientation $[1\ 1\ 1]$.

The diffractogram in Figure 18b with measured distances 1.12 nm^{-1} and 2.53 nm^{-1} and interplanar angle between $(2\ \bar{2}\ 0)$ and $(1\ 0\ 3)$ 76° was interpreted as $[3\ 3\ \bar{1}]$ zone axis of the Al_3Mn phase and the diffractogram in Figure 18c could be interpreted as $[\bar{4}\ 0\ 5]$ pole of the same structure supposing that every second spot in the planes $5X4$, where X is an integer, is invisible due to its low intensity. A set of reciprocal distances measured in the diffractograms obtained on the particle A were not found in any other possible structures formed in Al-Fe-Mn-Si systems. Therefore, the particle is most probably the Al_3Mn phase, even though the tilt angles between the diffractograms were not measured and their compliance could not be confirmed.

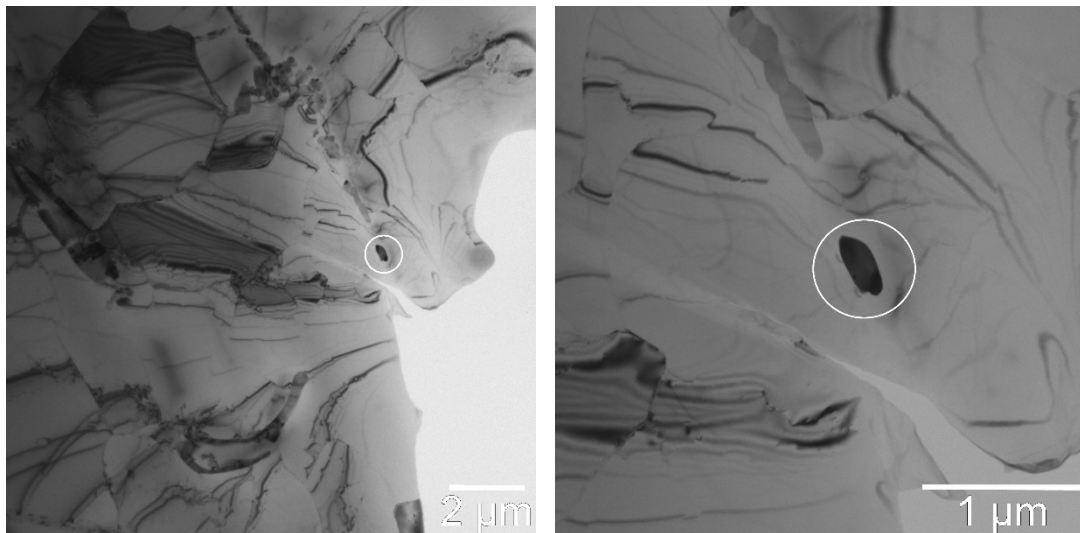


Figure 19: BF image of a dispersoid particle B used for phase evaluation.

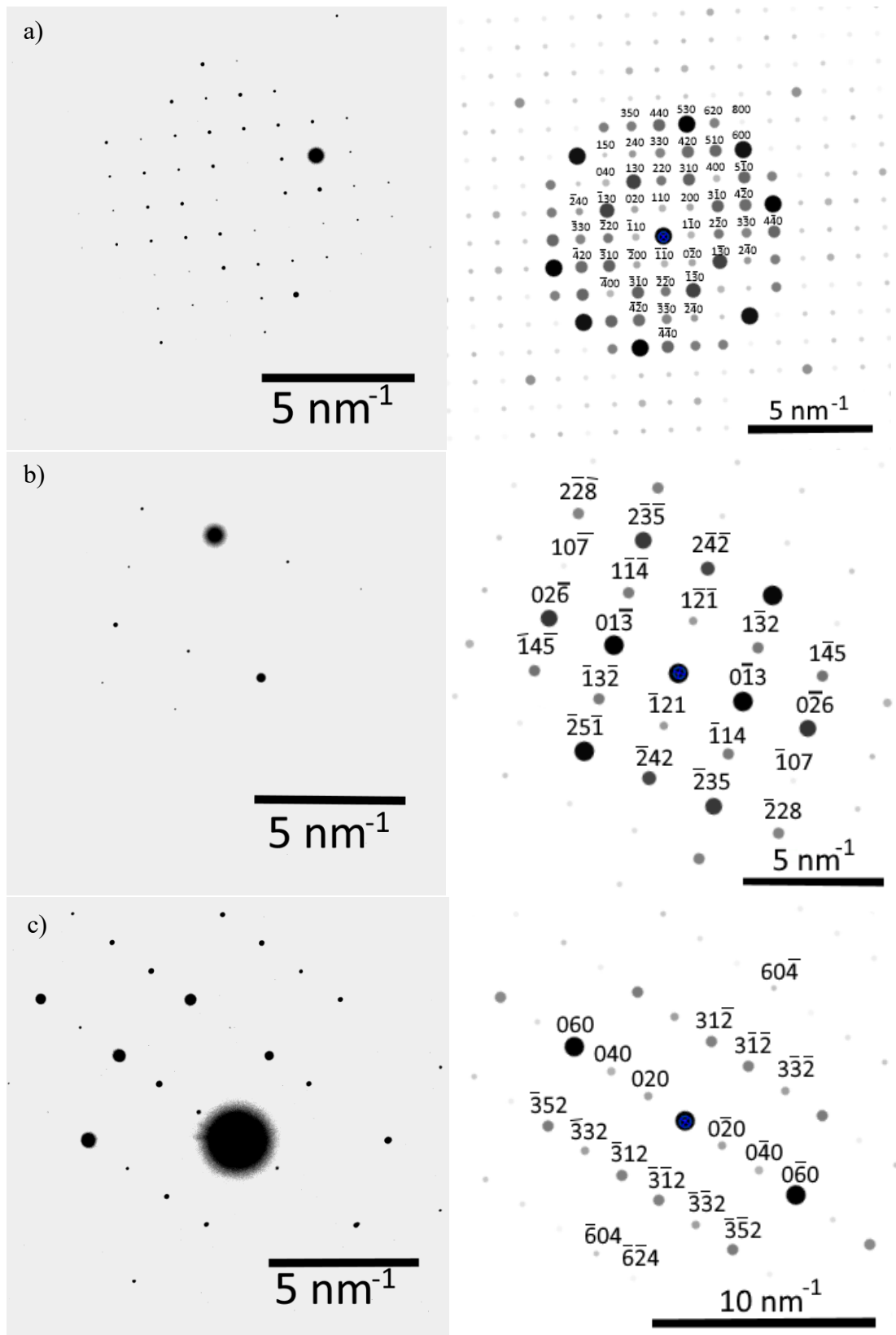


Figure 20: Diffractograms obtained from particle B and corresponding simulated patterns of α -Al(Fe,Mn)Si phase with following normal vectors: a) $[0\ 0\ 1]$, b) $[7\ 3\ 1]$, c) $[2\ 0\ 3]$.

All diffractograms obtained on particle B (Figure 19) correspond with simulated diffraction patterns of the body centered variant of cubic α -Al(Fe,Mn)Si phase. The square pattern formed in orientation [1 0 0] with the reciprocal distance $a^* = 1.12 \text{ nm}^{-1}$ (Fig. 20a) can be simulated also for Al_3Mn phase with the same orientation. Therefore, this orientation is not suitable for the determination of a proper phase. However, reciprocal distances of the diffractograms shown in the Figure 20b and 20c could not be found among the distances of Al_3Mn phase. Instead, the measured distances and angles correspond to the diffraction patterns of α -Al(Fe,Mn)Si phase in orientations [7 3 1] and [2 0 3]. Again, the compliance between the tilt angles while capturing diffractograms and the angles between interpreted orientations could not be confirmed but there is a high probability that the particle B corresponds to the body centered variant of cubic α -Al(Fe,Mn)Si phase.

Several different particles in the as cast state were also inspected but no more than one diffraction pattern from an orientation with a high value of Miller indices per particle was found. Therefore, the phases of the particles were not identified, however a frequent occurrence of a regular hexagonal pattern characteristic for the α -Al(Fe,Mn)Si suggests a prevalence of this phase in the material. On the contrary, the probability of the presence of Al_3Mn phase is low due to a small amount of Mn in the material, but it is also possible that atoms of Mn are substituted by Fe considering the commonly reported substitution of Mn with Fe in a variety of phases present in Al-Fe-Mn systems [15,18,57].

3.1.2 Annealed state

Analysis of the bright field image of the annealed sample shows that particles of a very similar shape and size as the ones in the material before annealing can be found (Fig. 21). Their occurrence is, however, scarcer and no large clusters are visible. Again, according to the shape of the particles, the presence of Al(Fe,Mn)Si phase or hexagonal Al_4Mn phase can be expected, however diffraction pattern evaluation is necessary.

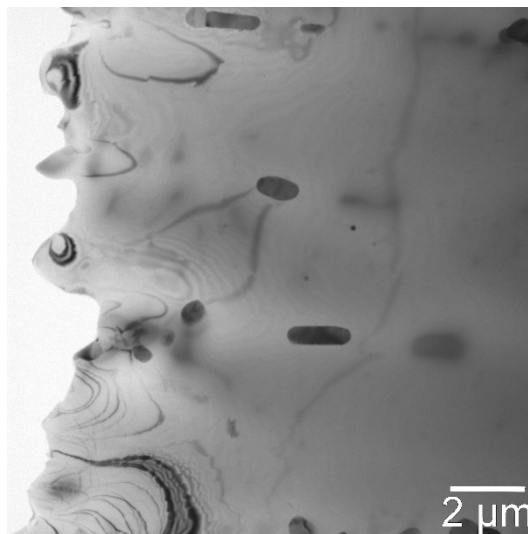


Figure 21: BF image of the AA1200 sample after annealing at 580° C for 4 hours.

Diffractograms taken from the particle in the Fig. 22 are shown in Fig. 23 along with their indexed patterns. A regular hexagonal pattern (Fig. 23a) with the reciprocal distance $a^* = 1.12 \text{ nm}^{-1}$ most likely corresponds to the [111] orientation of the cubic $\alpha\text{-Al(Fe,Mn)Si}$ phase. Since the matching simulated patterns of the same phase were also found for the other two diffractograms (Fig. 23 b,c), it is very probable that the particle indeed possesses this crystal structure. The phase has been reported as a stable one with no size and morphology changes during solution treatment between 495 °C up to 535 °C [57,58] which further supports our results.

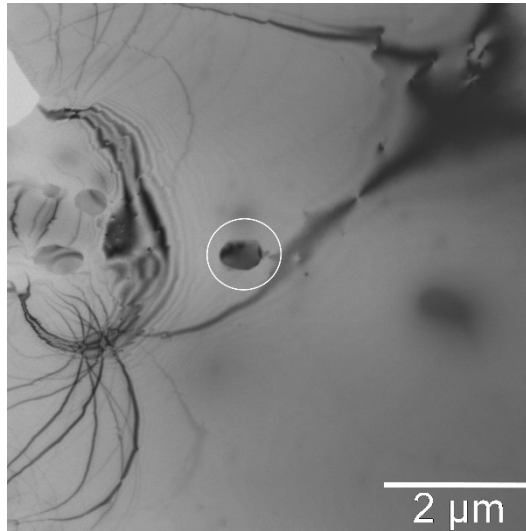


Figure 22: BF image of dispersoid particles in the annealed AA1200 sample used for the phase determination. The analyzed particle is marked by a circle.

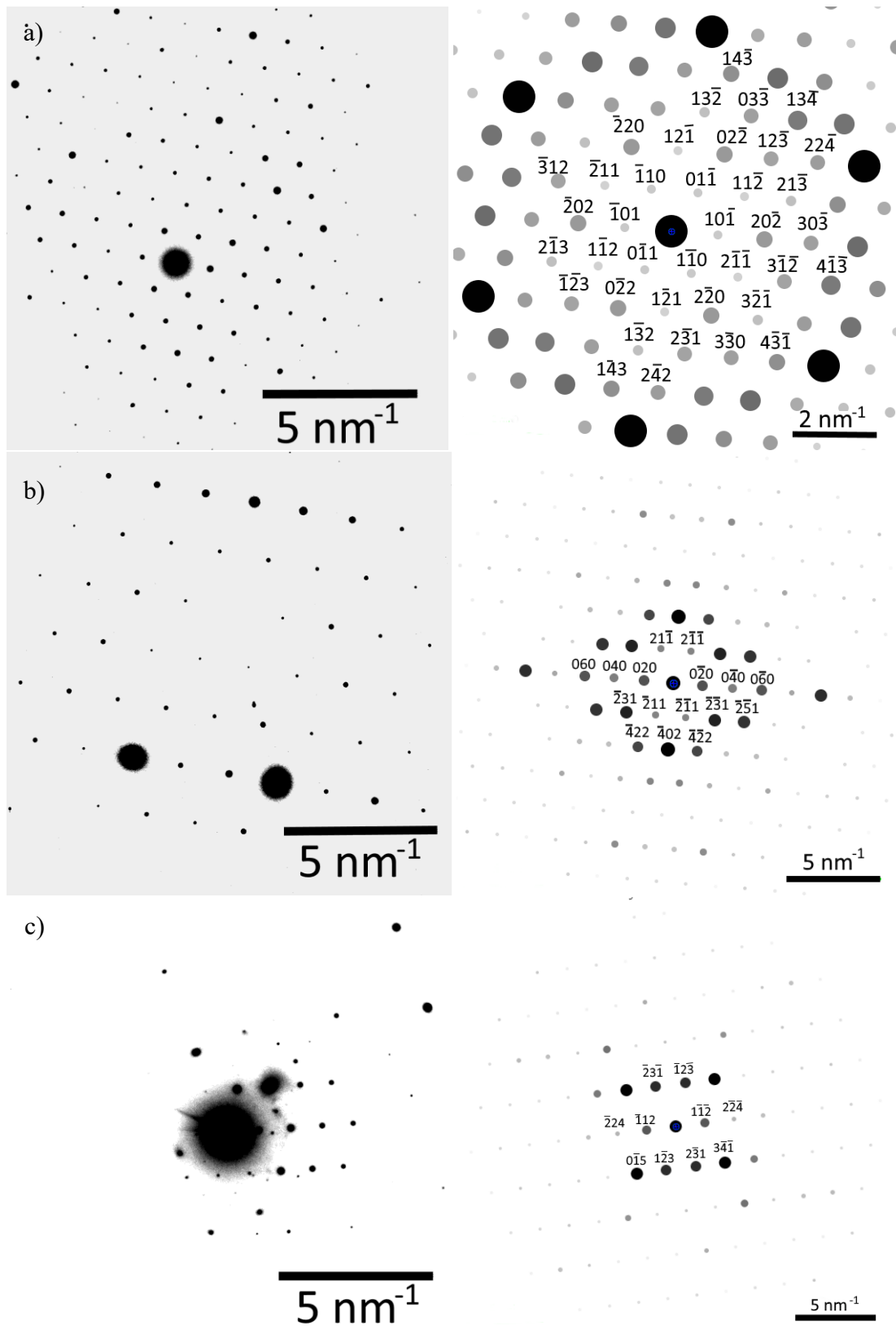


Figure 23: Diffractograms obtained from TEM and their corresponding simulated patterns of α -Al(Fe,Mn)Si phase with following normal vectors: a) $[1\ 1\ 1]$, b) $[1\ 0\ 2]$, c) $[7\ 5\ 1]$.

3.2 SEM analysis

In order to obtain more information about the distribution of dispersoids inside the sample and to find their chemical composition, backscatter-electron images of representative areas were taken and EDS analysis was performed on several particles before the realization of EBSD.

3.2.1 Backscatter-electron imaging

Detection of backscattered electrons is a standard method for the location of dispersoid particles in aluminum matrix in SEM. The intensity of electrons scattered back from the sample strongly depends on the atomic number of elements in the sample. Due to higher charge density in dispersoids, which are composed of elements with higher atomic number than aluminum, more electrons are backscattered and appear as bright areas in the acquired image [32]. Images of several areas under different magnifications were taken (Fig. 24) in order to receive more statistical information about dispersoid shape and distribution.

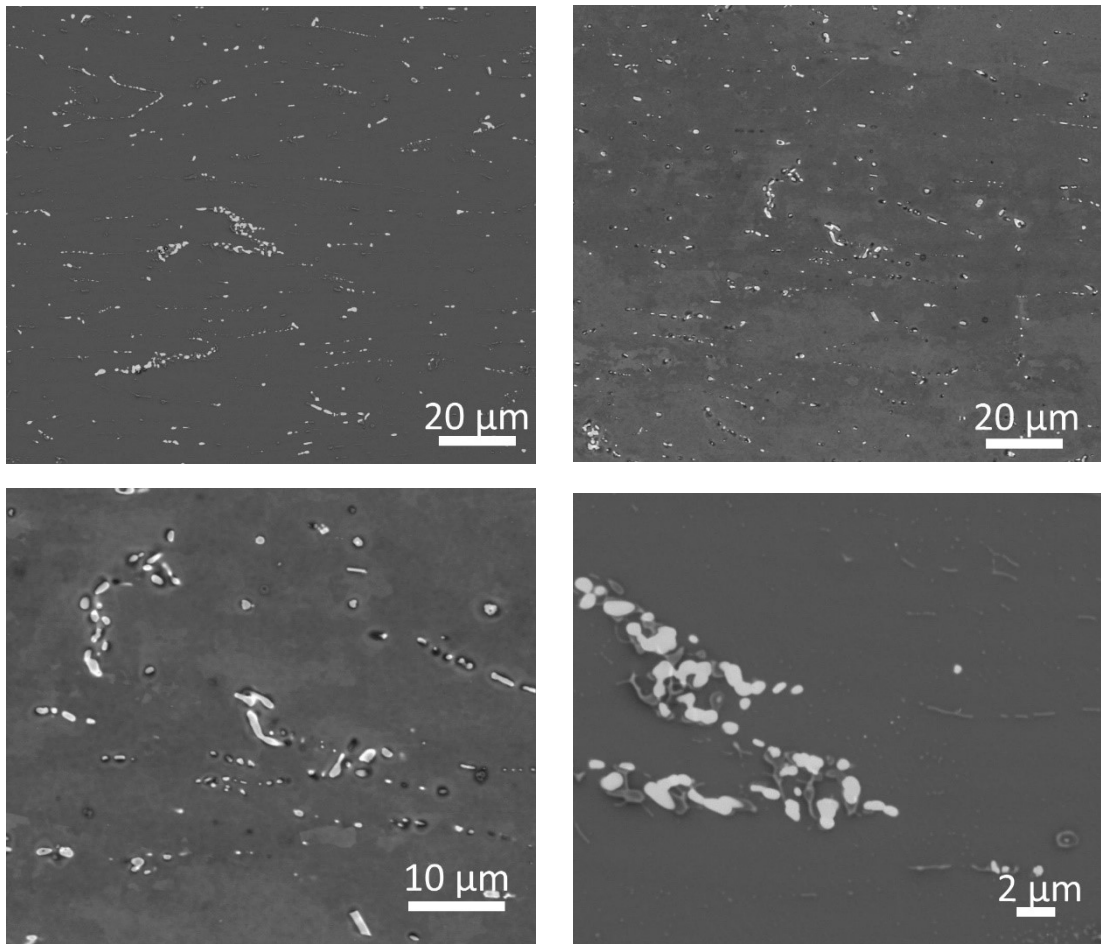


Figure 24: SEM backscattered electron images of AA1200 alloy annealed at 580 °C for 4 hours.

Backscattered electron images of the annealed sample reveal clusters of round or ellipsoidal particles evenly distributed over the surface of the specimen with shapes similar to the ones observed in the transmission electron microscope (Fig. 24). The size of the particles ranges from around 1 μm up to 5 μm .

3.2.2 EDS analysis

The EDS analysis (Fig. 25) of dispersoid particles shows a presence of the Al, Fe and Si with the composition given in Table 4.

Element/Line	a	b	c
FeL	34.6	30.8	27.9
AlK	59.5	65.9	68.0
SiK	5.9	5.2	4.0

Table 4: Composition of main constituents in three particles analyzed by EDS.

Several particles were arbitrarily chosen for the analysis and all of them give a similar composition. The compositions could reflect the presence of τ_6 , τ_5 phases or α -AlMnSi or β -AlMnSi phases with Mn atoms substituted by Fe. It is necessary to note that analysis of small particles in SEM might be strongly influenced by a presence of surrounding Al matrix. Considering the results obtained by the analysis of TEM diffraction patterns, the most probable phase the is α -Al(Fe,Mn)Si one.

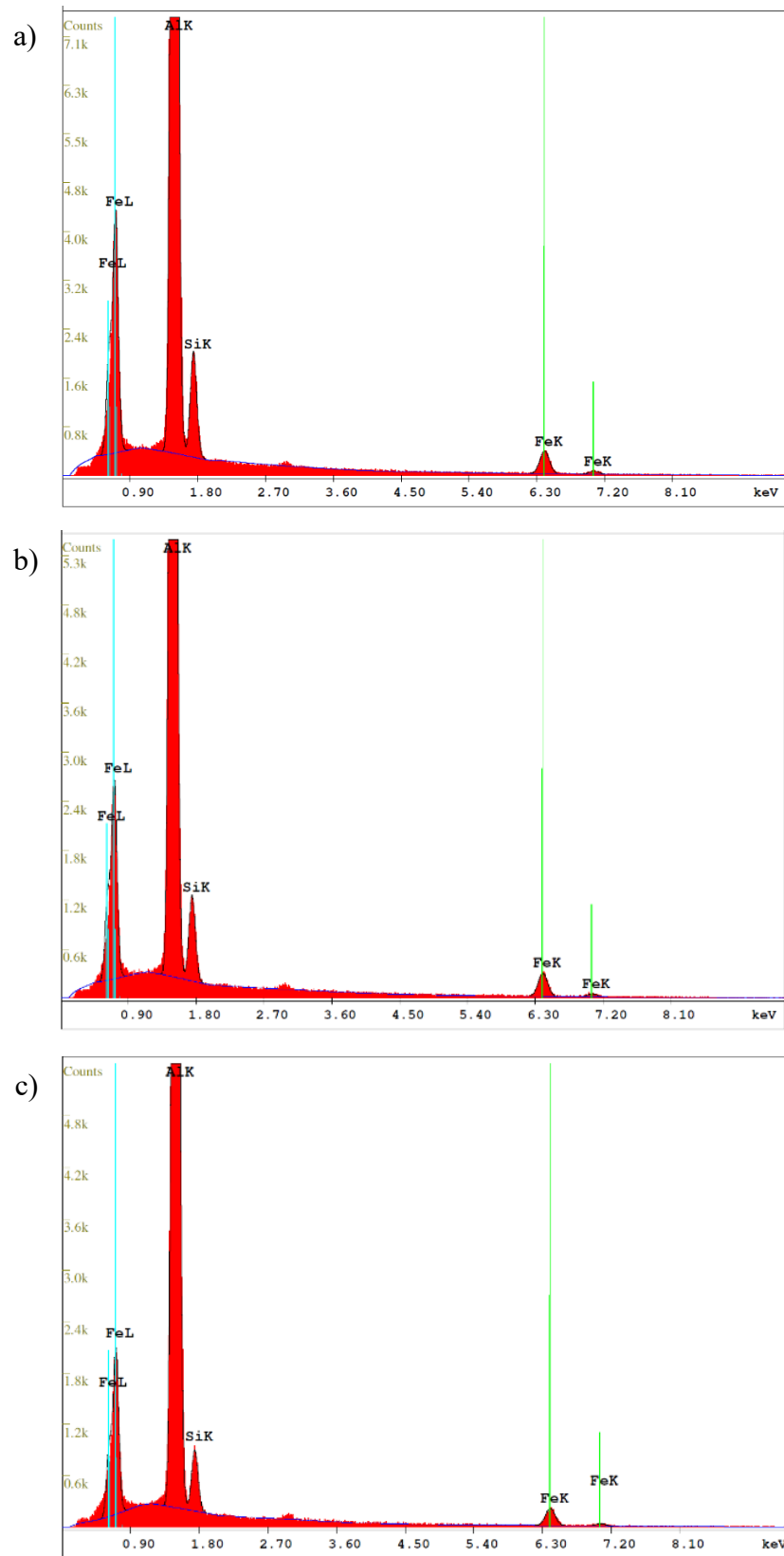


Figure 25: EDS analysis of three arbitrarily chosen particles.

3.2.3 EBSD evaluation

Finally, an EBSD analysis was performed on several areas containing dispersoid particles in order to determine their crystallographic structure and orientations. Respecting the results of TEM evaluation, only the phases α -Al(Fe,Mn)Si (cubic) and Al_3Mn (orthorhombic) were considered.

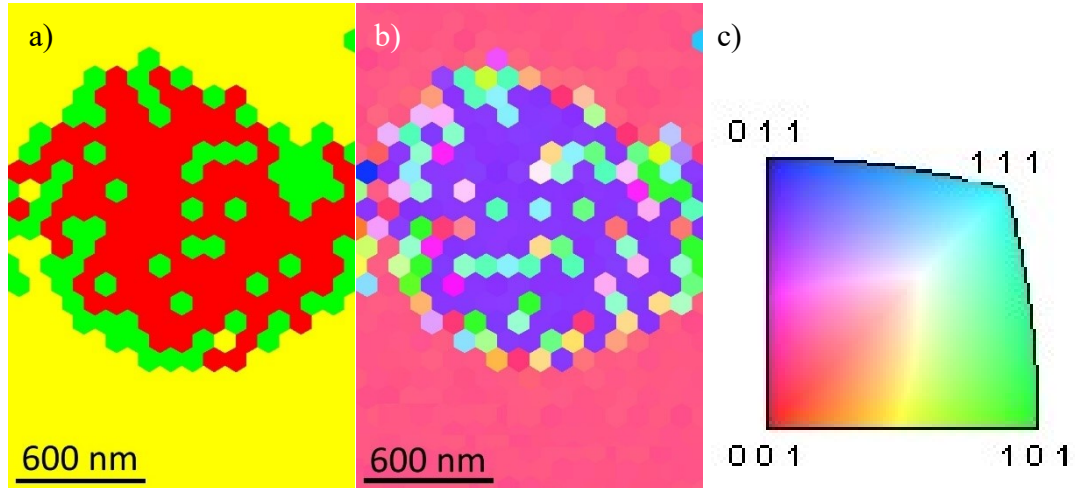


Figure 26: a) EBSD phase evaluation of a dispersoid particle in the aluminum matrix (yellow: Al, green: Al_3Mn , red: α -Al(Fe,Mn)Si), b) inverse pole figure map of the same particle indexed using α -Al(Fe,Mn)Si phase, c) orientation color code map for α -Al(Fe,Mn)Si phase.

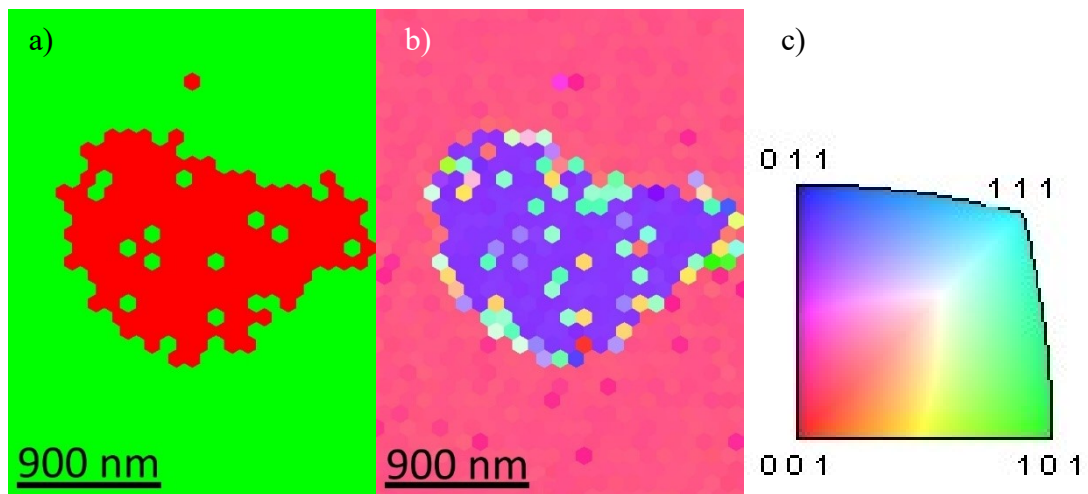


Figure 27: a) EBSD phase evaluation of a dispersoid particle from Fig. 26 without Al_3Mn phase (green: Al, red: α -Al(Fe,Mn)Si), b) inverse pole figure map of the same particle indexed using α -Al(Fe,Mn)Si phase, c) orientation color code map for α -Al(Fe,Mn)Si phase.

EBSD analysis considering the phases Al_3Mn and α -Al(Fe,Mn)Si (Fig. 26) of a chosen dispersoid in an aluminum matrix can reliably index the pure aluminum part of the scanned area and inclines to the α -Al(Fe,Mn)Si phase as a more probable phase forming the particle. The randomly distributed dots interpreted as Al_3Mn inside the particle are evidently errors made by the automatic evaluation system. Similarly, the dots significantly different from its surroundings on inverse pole figure are clearly not

correct. When taking into an account only α -Al(Fe,Mn)Si phase (Fig. 27), the results are improved and a smaller number of evidently erroneously evaluated spots appear. However, such clear results could be obtained only after a long search for a suitable particle inside the material. When scanning a larger area containing more particles (Fig. 28) or even when scanning different similarly shaped and sized particles, the correct phase could not be unambiguously determined. The phase evaluation algorithm may not have had any problems with distinguishing between the pure aluminum and more complex cubic α -Al(Fe,Mn)Si phase, but the orientation map of the particle area is disorganized thus the orientation can not be determined with a sufficient probability.

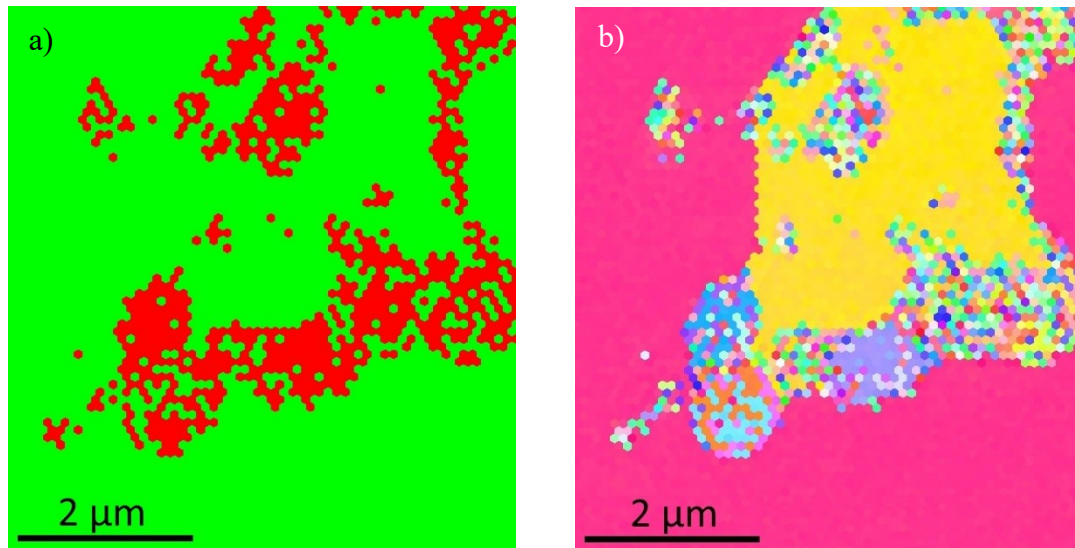


Figure 28: a) EBSD phase evaluation of dispersoids in the aluminum matrix (green: Al, red: α -Al(Fe,Mn)Si), b) EBSD inverse pole image of the same area.

To analyse the miscalculation in the phase orientation, the Kikuchi patterns were closely examined (Fig. 29). For every captured pattern, several highly probable orientations were proposed and the most probable one was chosen and drawn into the orientation map. The analyzed Kikuchi patterns (Fig. 29b–d) differ mainly in the position of the yellow Kikuchi lines. However, a closer look on the non-fitted pattern (Fig. 29a) exhibits no truly visible lines corresponding to the yellow ones.

Angles calculated between normals of a) and b), a) and c) and b) and c) are 101° , 102° and 35° respectively (Fig. 29). Angles between calculated normals were evaluated for several particles but no visible pattern or relation between them was discovered, unlike the angles between the five probable orientation solutions observed by Becker [47] (see par. 1.5.1). The ambiguity is most probably a result of a poor quality of the obtained Kikuchi line patterns, which is probably caused by a small size of the particles and their overlapping by the surrounding aluminum matrix.

Well defined Kikuchi lines are visible in pictures taken in the aluminum matrix (Fig. 30). In comparison to simulated α -Al(Fe,Mn)Si patterns the fitting of the simulated aluminum ones is better and the phase and orientation evaluation runs smoothly.

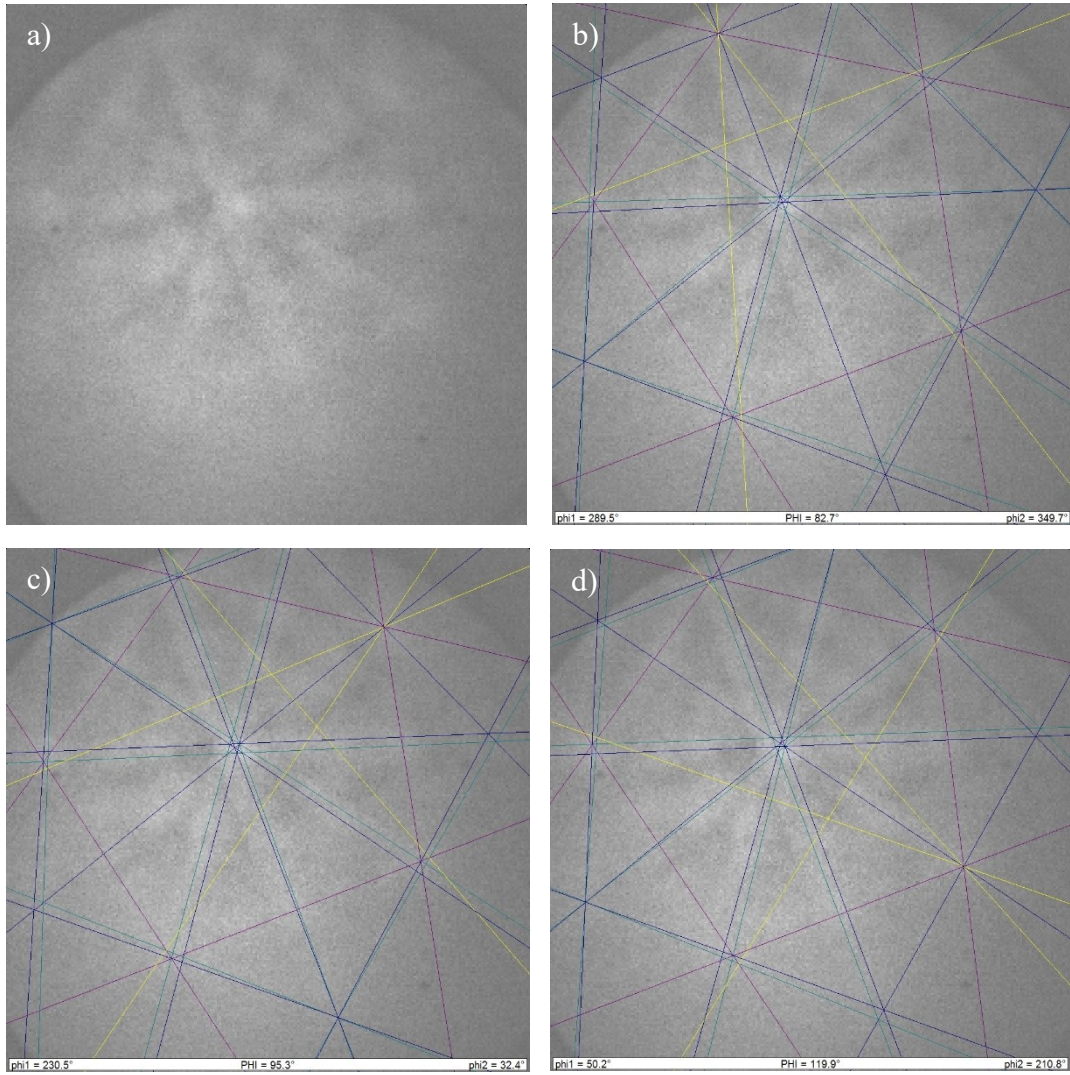


Figure 29: a) A Kikuchi pattern obtained in one point of the EBSD scan in the dispersoid particle, b) – d) simulated Kikuchi patterns for three most probable orientations of the particle.

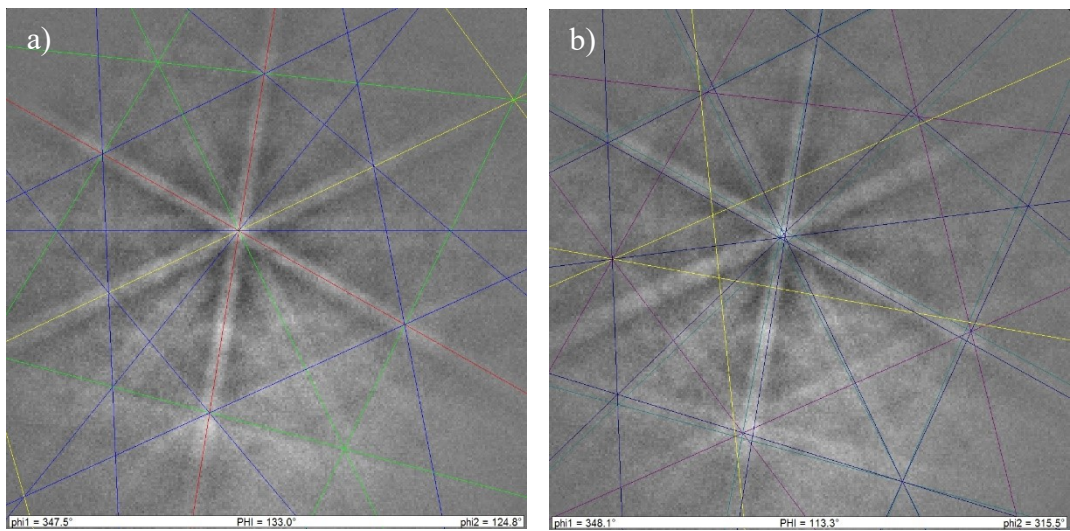


Figure 30: Simulated Kikuchi pattern of a) aluminum, b) α -Al(Fe,Mn)Si, fitted on the aluminum pattern captured in one point of the EBSD scan.

3.3 ASTAR

Automated orientation crystal phase and orientation mapping was realized on a cluster of particles shown in Figure 31. Similarly as in EBSD analysis only Al_3Mn and $\alpha\text{-Al(Fe,Mn)Si}$ templates were calculated and fitted with experimental patterns.

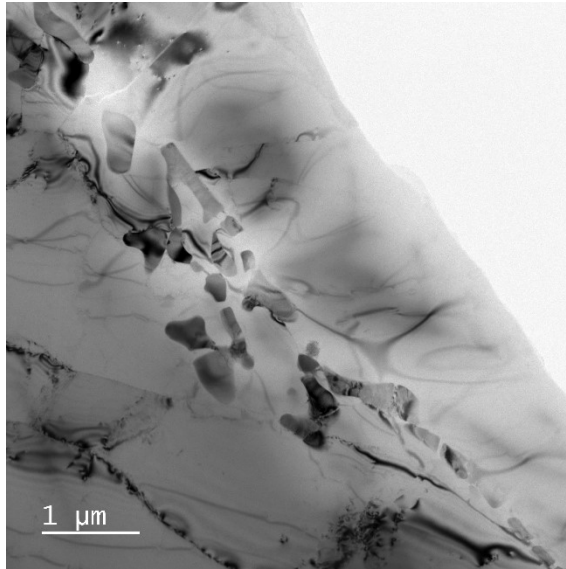


Figure 31: a) Bright field image of a cluster of particles used for further observations.

EDS mapping of an area of the annealed sample containing a cluster of dispersoids confirmed a presence of Al, Fe and Si in the particles, and naturally, a presence of Al in the whole studied area. The results are consistent with the ones obtained by EDS analysis in SEM. Color maps represent the distribution of main elements in the material.

The same area was afterwards analyzed using automated ASTAR method (Fig. 33) with a standard camera length 20 cm suitable for the analysis of a majority of metals. Both Al_3Mn and $\alpha\text{-Al(Fe,Mn)Si}$ cubic phase structures were considered as a possible options during evaluation, however a majority of the area of the particles was identified as $\alpha\text{-Al(Fe,Mn)Si}$. Therefore, only this structure was finally used for the orientation analysis. Only the orientation of aluminum matrix was clearly determined, whereas inside the dispersoids, rather unacceptable random orientations were indicated (see Fig. 33).

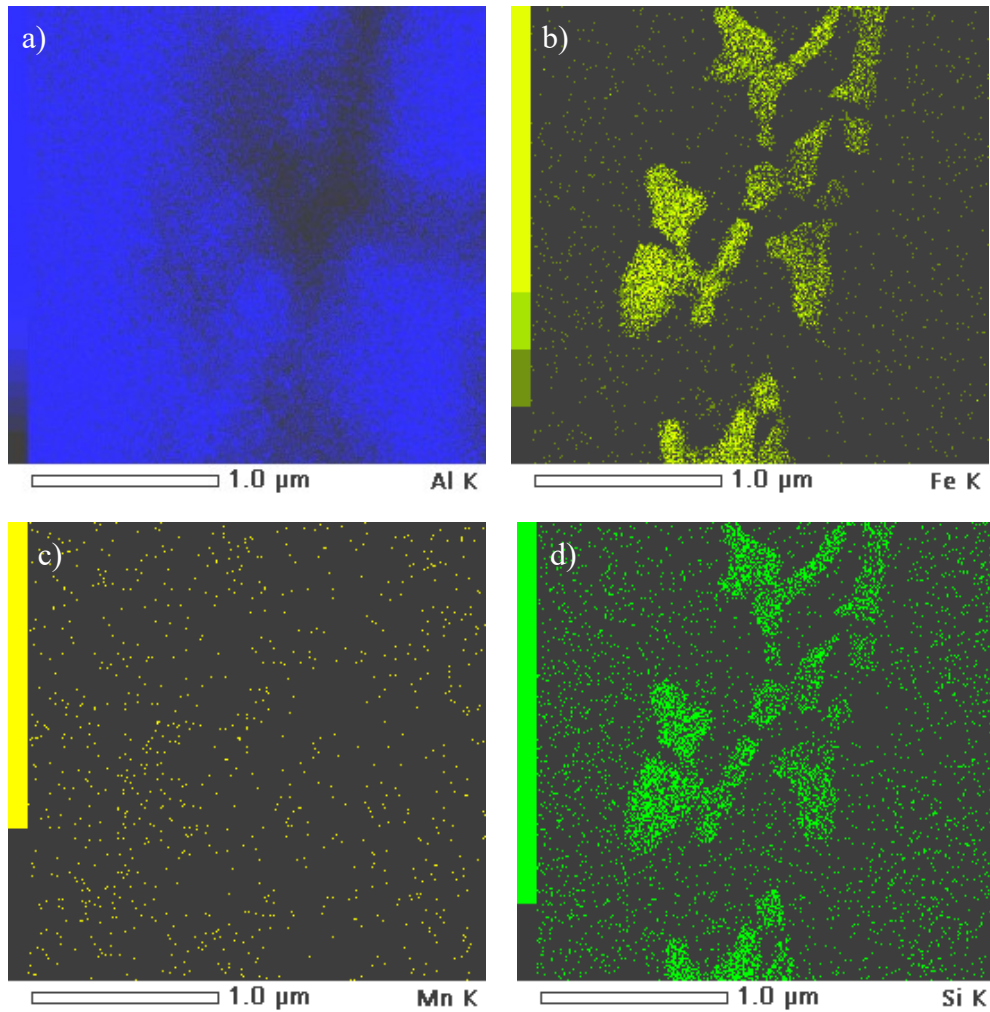


Figure 32: EDS maps of main constituents in dispersoids from Fig. 30.

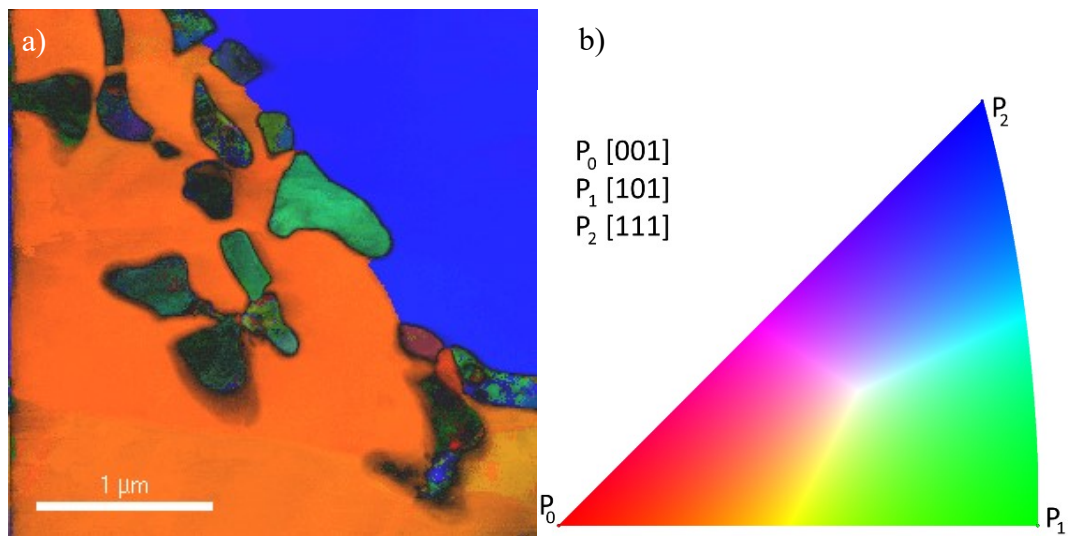


Figure 33: a) Inverse pole figure of the annealed sample obtained by ASTAR analysis using a small camera length, b) orientation triangle of a cubic structure.

In order to find the cause of the ambiguity, the automated matching between the calculated templates and the obtained diffractograms were manually examined (Fig. 34). It is evident that in contrast to pure aluminum with diffraction spots reasonably remote, the large lattice parameter of the α -Al(Fe,Mn)Si cubic phase caused their

indistinguishably close distribution making a correct interpretation of the diffraction pattern impossible.

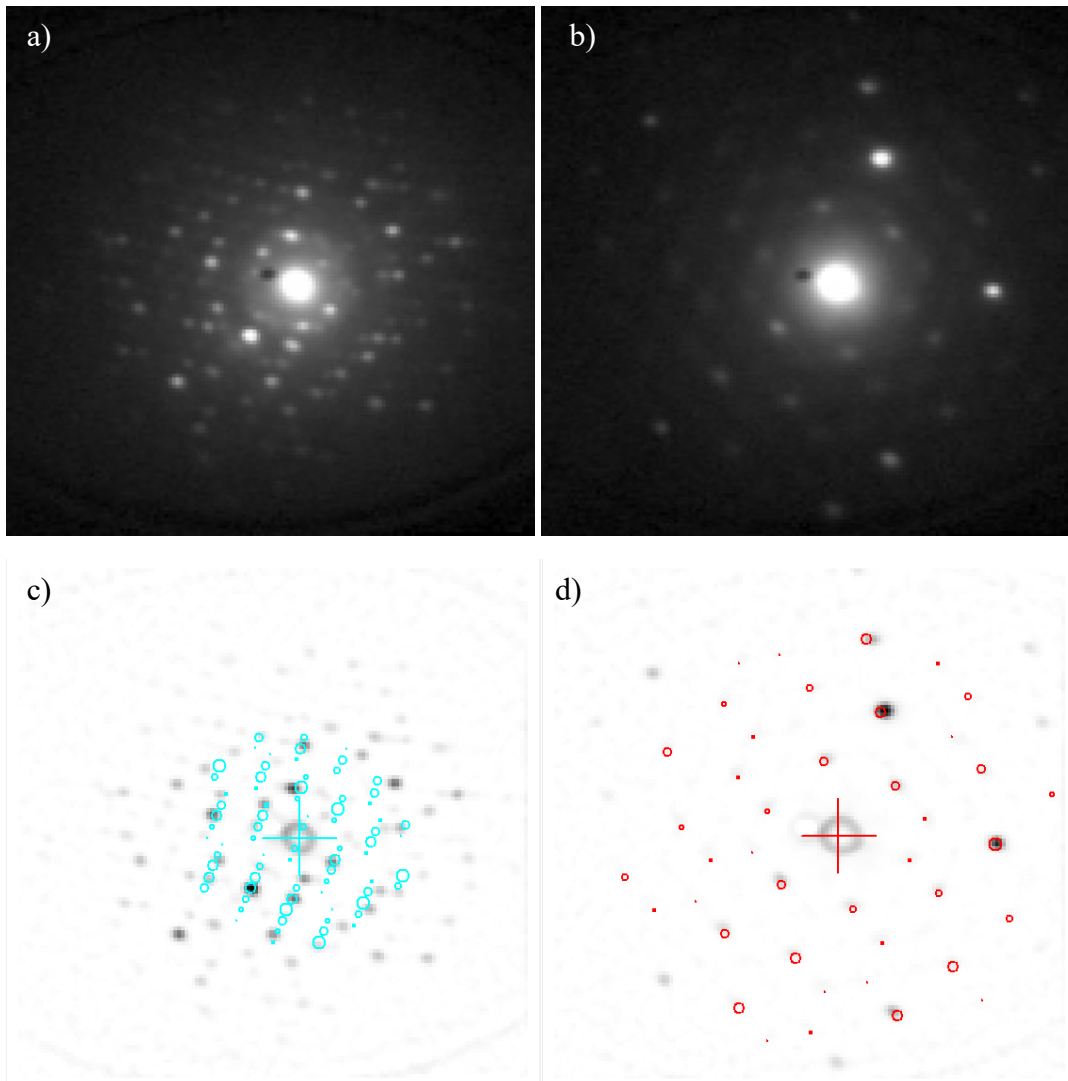


Figure 34: A comparison of diffraction patterns and their matched templates for the particle a), c) and aluminum b), d).

In an attempt to increase distances between diffraction spots in patterns obtained from particles and hereby facilitate their evaluation, the camera length was increased. To test this approach, only 50x50 points large area was scanned, leaving the resulting images with a slightly lower resolution (Fig. 35).

The examination of Figure 35 reveals that the orientation found throughout the whole particles is uniform therefore it finally gives a reliable result. On the other hand, the orientation of the aluminum matrix is now disintegrated (Fig. 35 c). Moreover, the shape and the size of particles in an apparent bright field shows (Fig. 36) that the area behind the yellow borders indicating the original size of the particles (Fig. 36b) belongs to the aluminum matrix. Therefore, the templates matching was examined again manually (Fig. 37-41).

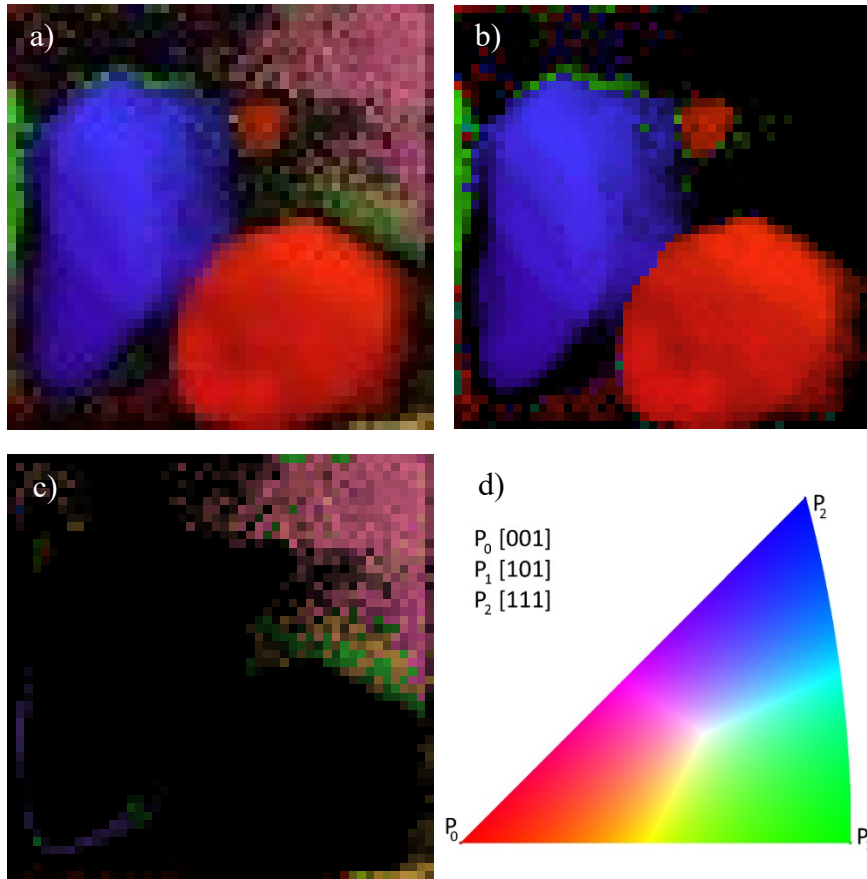


Figure 35: Inverse pole figures of the annealed sample area obtained through ASTAR analysis using larger camera length a) aluminum and α -Al(Fe,Mn)Si particles, b) only α -Al(Fe,Mn)Si particles, c) only aluminum, d) orientation triangle.

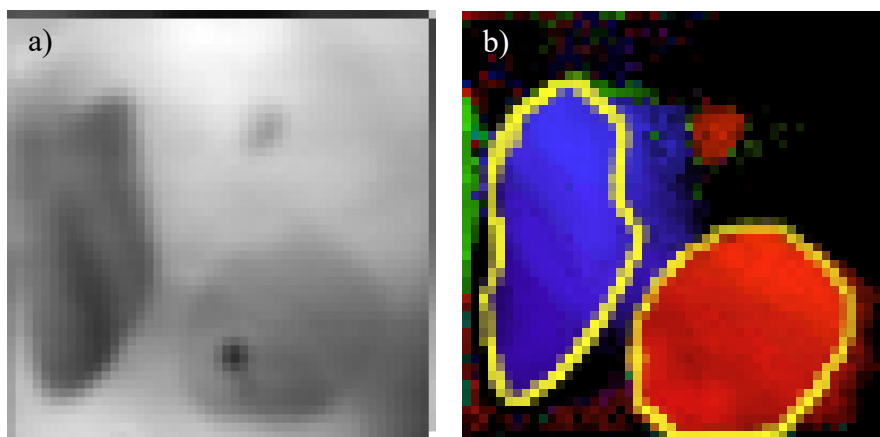


Figure 36: Comparison of apparent bright field (intensity of transmitted primary beam) with an orientation map of the same area.

Diffractograms were taken from points (i) inside the particle, (ii) in the aluminum in the vicinity of the particle, and (iii) in the aluminum further away from the particles (indicating on Fig. 37a-c) were taken. As can be seen in Fig. 37d-f, the diffraction spots captured inside the particle are visible also on scans performed inside the aluminum matrix. This fact is an artefact caused by the detector capturing

diffractograms. Due to a long relaxation time of the luminophore the screen still carries the information of previously captured images even though the scanning beam has already moved. To resolve the problem, a new camera with shorter relaxation time or longer period between two scans are necessary.

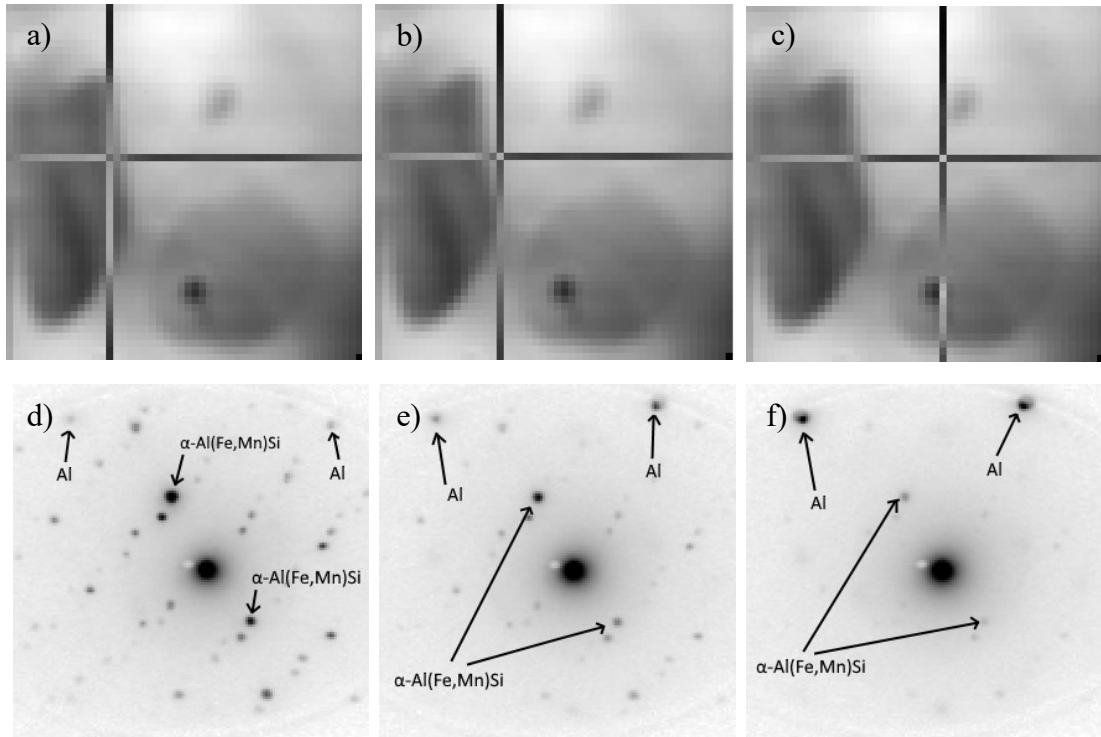


Figure 37: a)-c) simulated bright field, d)-f) corresponding diffractograms.

The interpretation of diffractograms received from particles is enhanced due to the presence of reflections from higher Laue zones. Template matching inside both particles using large camera length yields plausible results and the orientation triangles give one definite most probable orientation (Fig. 38). In Figure 39c, however, dark grey bands indicating several probable orientations can be noticed. This is a consequence of an existence of two intensive bright spots in the diffraction pattern marked by arrows in Fig. 39b, which are present in all templates representing the dark grey bands. This strong intensity is responsible for a high value of the correlation index (eq. 9). However, the presence of the remaining finer diffraction spots from higher Laue zones ensures the assignment of the correct template.

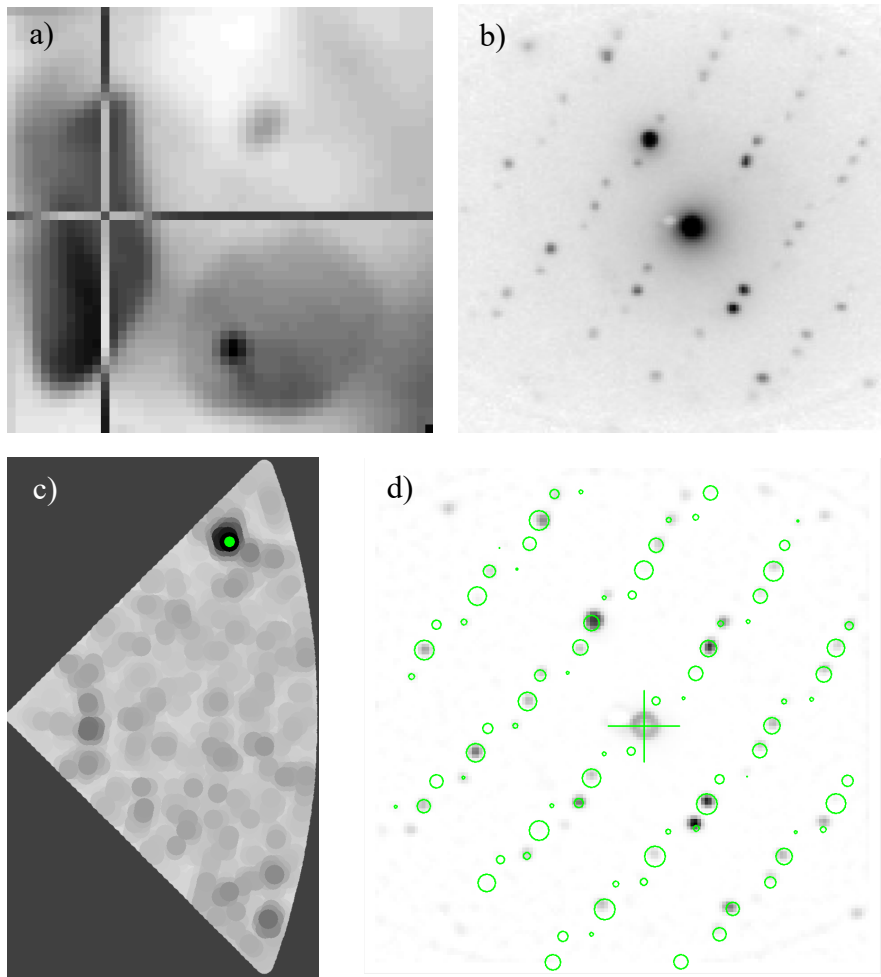


Figure 38: Template matching inside one of the particles: a) simulated bright field with a spot in the particle where the diffractogram was taken, b) obtained diffractogram, c) orientation triangle, d) matched template.

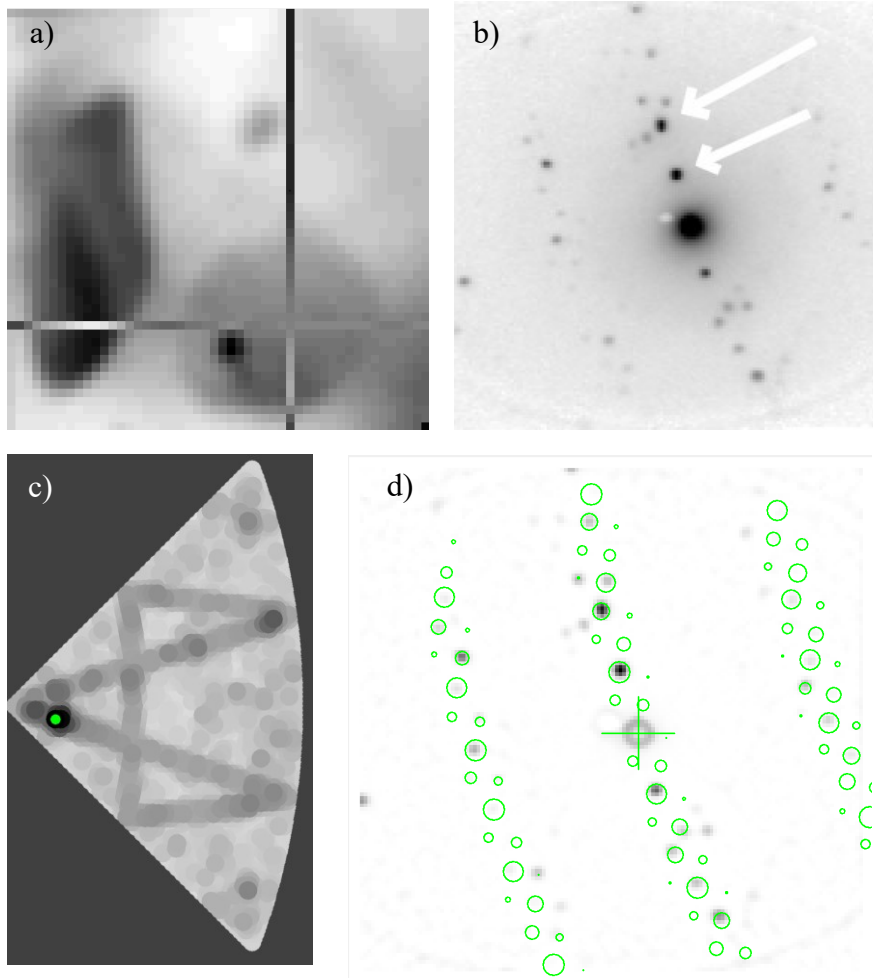


Figure 39: Template matching inside one of the particles, a) – d) analogical to the description under Figure 38.

The orientation triangle in Figure 40c, holds a pattern similar to the one in the Figure 38, but larger amount of orientations is marked as a highly probable and they are almost equally possible. A closer look on the diffractogram (Fig. 40b) shows that only one intensive bright spot marked by arrow (representing one system of equivalent planes) and a few paler ones are visible. The remaining spots necessary to evaluate the diffraction pattern are fairly more distant from the center and were not captured by the camera. This limited number of diffraction spots in the Al matrix (consequence of larger camera length) is responsible for the ambiguity of orientations in the final image.

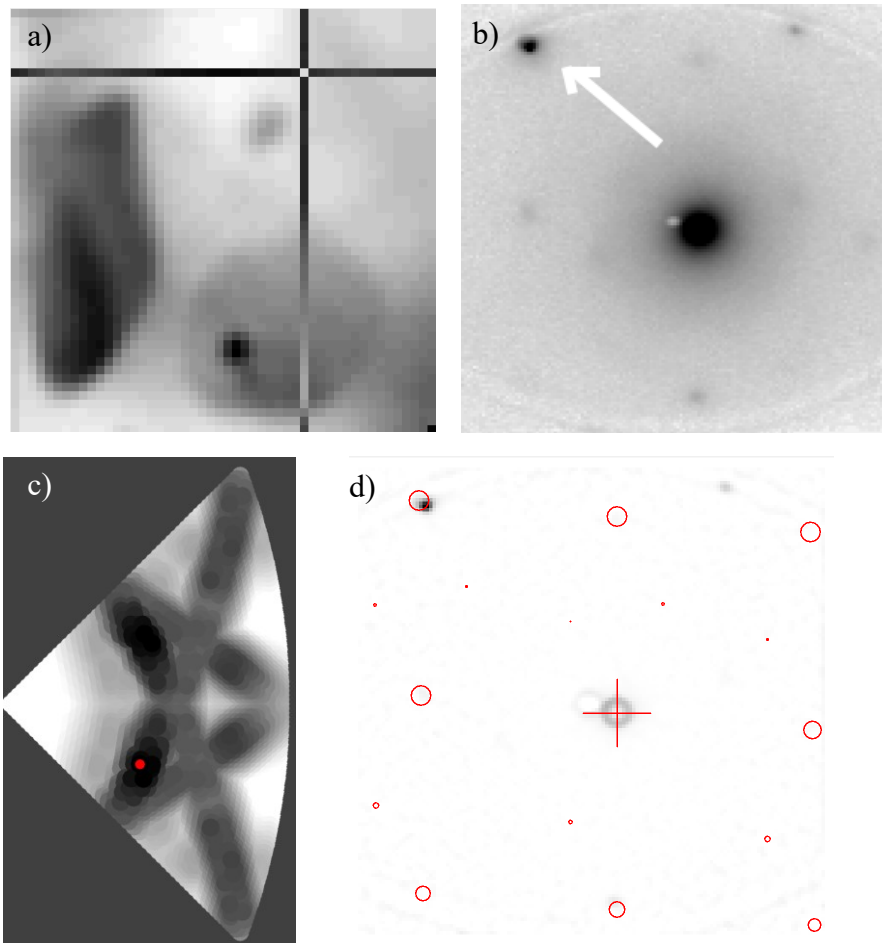


Figure 40: Template matching inside aluminum matrix, a) – d) analogical to the description under Figure 38.

The absence of additional diffraction spots plays role also in the diffraction interpretation shown in Figure 41. In this case the most probable orientations are not lying on the same trace connected to a single plane but are randomly distributed (Fig. 41c).

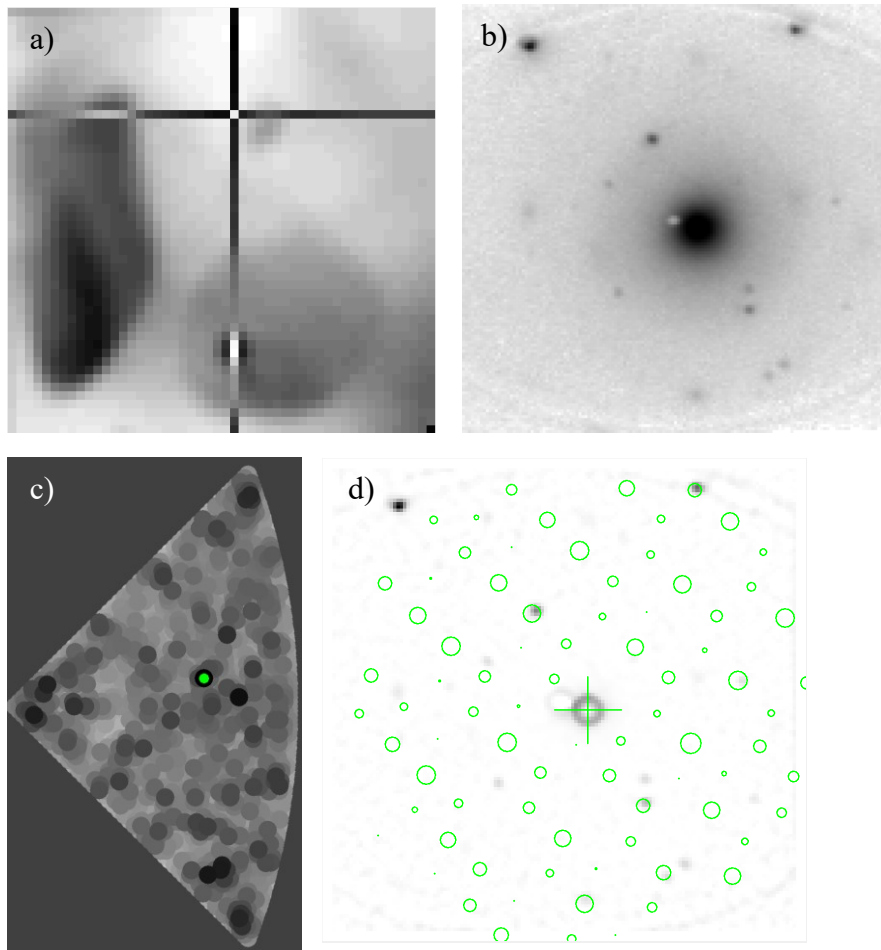


Figure 41: Template matching inside aluminum, a) – d) analogical to the description under Figure 38.

Plotting a line of misorientations across particles (Fig. 42a,b) into a stereographic projection shows four unrecognisable equivalent orientations for both particles marked by blue (Fig. 42d) or red (Fig. 42e) squares. According to the orientation triangle (Fig. 35d), the orientation of a crystal structure of one particle is near the crystal zone $[111]$ parallel to the electron beam (blue) and the orientation of the second particle is near the zone $[001]$ (red).

Slightly delocalised clusters of squares indicate that the resultant orientations are not precisely in one direction of the pole figure, but rather scattered in the vicinity of the four equivalent orientations. This effect confirms a high angular resolution of this method because diffractograms taken from a crystal under nearly the same orientation are in general the same. They differ only in small variations of intensities of diffraction spots not recognisable to a human eye.

A small number of points inside particles, marked by black symbols (Fig. 42e), were evaluated with a very low confidence index. However a small number of errors is not decisive since the main strength of the technique lays in a statistical evaluation of a large number of diffractograms instead of precise evaluation of each of them. Moreover, averaging and cleaning methods known from EBSD could plausibly suppress the presence of such points increasing thus a statistical credibility of the

analysis. Orientations of aluminum matrix are far more diverse (Fig. 42f) for the reasons already explained above.

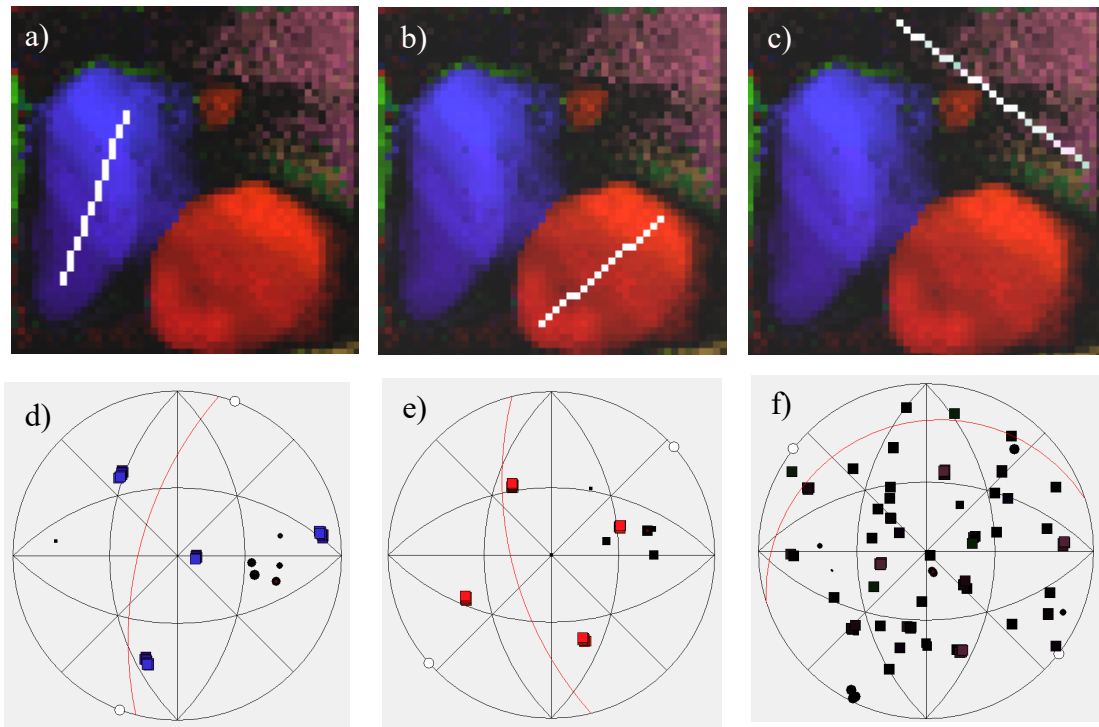


Figure 42: Inverse pole figures with marked lines along which the orientations of [111] zones were calculated a)-c) and plotted in stereographic projections d)-f).

Conclusions

Three different methods of crystallographic structure identification and orientation based on Bragg analysis (SAED and ASTAR) and Kikuchi analysis (EBSD) were tested on small intermetallic particles from the quaternary Al-Fe-Mn-Si system.

Phase and orientation evaluations through diffractograms obtained in SAED mode in TEM were performed on both as cast and annealed states of TRC AA1200 aluminum alloy. Two different phases Al_3Mn and body centered $\alpha\text{-Al}(\text{Mn},\text{Fe})\text{Si}$ were identified in the as cast state. Analysis of a number of different particles and small amount of Mn present in the material indicate more probable occurrence of the $\alpha\text{-Al}(\text{Mn},\text{Fe})\text{Si}$ phase, however, since the SAED analysis requests a complex diffractogram analysis for several tilts of each particle, the statistical examination of particles orientation and the type distribution is rather challenging.

The application of the EBSD technique based on a Kikuchi analysis is rather problematic most probably because of a narrow shape and a small size of the particles. The Kikuchi patterns formed on particles were generally overshadowed by a more pronounced lines originating from a surrounding aluminum matrix resulting in a misinterpretation of acquired patterns. The situation is much worse in the case of the cast strip because the particle size is much smaller than in the annealed one. Therefore, EBSD method is probably not suitable for the crystallographic evaluation of particles smaller than 1 μm .

The ASTAR system was tested on the annealed state of the material. A simultaneous analysis of structures with considerable different lattice parameters did not produce reasonable results, due to a significant difference in the density of diffraction spots, which were either too close and undisguisable by the system or on the contrary too scarce so that a correct evaluation suffered from a large experimental error. The adjustment of a camera length allows to focus on a certain range of lattice parameters because the parameters of a majority of intermetallic phases present in the Al-Fe-Mn-Si systems are of a comparable length. Only the parameters of aluminum and Al_3Fe are considerably shorter. For that reason, the identification of phases and their orientations can be performed in two steps consisting of acquisition of two maps under two different camera lengths. The optimization of the camera length for both sets of lattice parameters is an option which should also be taken into a consideration. The above-mentioned approaches are more challenging, but they are still incomparably more effective than the analysis based on a systematic inspection of suitable diffractograms separately for each particle in the SAED mode in TEM. One of the main advantages of the automated template matching is the possibility to avoid the complicated and time demanding orientation of particles into highly symmetric directions, which makes the whole evaluation process considerably more effective. An identification ambiguity may appear in a case of a very similar diffraction patterns of two different phases for certain orientations such as $[0\ 0\ 1]$ orientation of $\alpha\text{-AlMnSi}$ phase and Al_3Mn phase. Therefore, repeated scanning of the sample tilted to several different angles may increase a probability of a correct phase identification.

The identified body centered α -Al(Fe,Mn)Si phase in the annealed state, which is in accordance with the literature findings reported as a stable one, further supports the plausibility of the method as an effective tool for the statistical analysis of dispersoids in Al-Fe-Mn-Si system. A repetition of this method over a large area could provide sufficient statistically convincing data.

Bibliography

1. STAN-GŁOWIŃSKA, K., LITYŃSKA-DOBRYŃSKA, L., MORGIEL, J., GÓRAL, A., GORDILLO, M. A. and WIEZOREK, J. M. Enhanced thermal stability of a quasicrystalline phase in rapidly solidified Al-Mn-Fe-X alloys. *Journal of Alloys and Compounds*. 2017. Vol. 702, p. 216–228.
2. CHO, S. S., CHUN, B. S., WON, C. W., KIM, H. K., LEE, B. S., YIM, K. H., SSAIN, E., BAEK, H., SONG, B. J. and SURYANARAYANA, C. Microstructure and Mechanical Properties of Rapidly Solidified Hypereutectic Al–Si and Al–Si–Fe Alloys. *Journal of Materials Synthesis and Processing*. 1998, Vol. 6., p. 123–131.
3. ZHAO, Q., HOLMEDAL, B. and LI, Y. Influence of dispersoids on microstructure evolution and work hardening of aluminium alloys during tension and cold rolling. *Philosophical Magazine*. 2013. Vol. 93, p. 2995–3011.
4. MUGGERUD, A. M. F., LI, Y. J. and HOLMESTAD, R. Orientation Studies of α -Al(Fe,Mn)Si Dispersoids in 3xxx Al Alloys. *Materials Science Forum*. 2014. Vol. 794-796, p. 39–44.
5. ROUVIMOV, S., RAUCH, E. F., MOECK, P. and NICOLOPOULOS, S. Automated Crystal Orientation and Phase Mapping of Iron Oxide Nano-Crystals in a Transmission Electron Microscope. *Microscopy and Microanalysis*. 2009. Vol. 15, p. 1290–1291.
6. KRATOCHVÍL, P., LUKÁČ, P. and SPRUŠIL, B. *Úvod do fyziky kovů I*. SNTL/ALFA, 1984.
7. KITTEL, Charles. *Thermal physics*. W. H. Freeman, 1980.
8. CALLEN, Herbert B. *Thermodynamics and an Introduction to Thermostatistics, 2nd Edition*. John Wiley & Sons, 1985.
9. MALLIK, A. K. Computer calculations of phase diagrams. *Bulletin of Materials Science*. 1986. Vol. 8, p. 107–121.
10. LIU, Z. K., CHANG, A. Thermodynamic Assessment of the Al-Fe-Si System. *Metallurgical and Materials Transactions A*. 1999. Vol. 30, p. 1081–1095.
11. CHEN, H., et al. Update of Al–Fe–Si, Al–Mn–Si and Al–Fe–Mn–Si thermodynamic descriptions. *The Transactions of Nonferrous Metals Society of China*. 2014. Vol. 24, p. 2041–2053.
12. RAGHAVAN, V. Al-Fe-Mn-Si (Aluminum-Iron-Manganese-Silicon). *Journal of Phase Equilibria and Diffusion*. 2007. Vol. 28, p. 215–217.
13. DU, Y., SCHUSTER, J. C., LIU, Z. K., HU, R., NASH, P., SUN, W., ZHANG, W., WANG, J., ZHANG, L., TANG, Ch., ZHU, Z., LIU, S., OUYANG, Y., ZHANG, W. and KRENDELSBERGER, N. A thermodynamic description of the Al–Fe–Si system over the whole composition and temperature ranges via a hybrid approach of CALPHAD and key experiments. *Intermetallics*. 2008. Vol. 16, p. 554–570.
14. GHOSH, G. Aluminium – Iron – Silicon. *Iron Systems, Part 1 Landolt-Börnstein - Group IV Physical Chemistry*. 2008. p. 184–266.

15. ZHENG, W., MAO, H., LU, X. G., HE, Y., LI, L., SELLEBY, M. and ÅGREN, J. Thermodynamic investigation of the Al-Fe-Mn system over the whole composition and wide temperature ranges. *Journal of Alloys and Compounds*. 2018. Vol. 742, p. 1046–1057.
16. DU, Y., JIN, Z., HUANG, B., GONG, W., XU, H., YUAN, Z., SCHUSTER, J. C., WEITZER, F. and KRENDELSBERGER, N. A thermodynamic description of the Al-Mn-Si system over the entire composition and temperature ranges. *Metallurgical and Materials Transactions A*. 2004. Vol. 35, p. 1613–1628.
17. BALITCHEV, E., JANTZEN, T., HURTADO, I. and NEUSCHÜTZ, D. Thermodynamic assessment of the quaternary system Al–Fe–Mn–Si in the Al-rich corner. *Calphad*. 2003. Vol. 27, p. 275–278.
18. LACAZE, J., ELENO, L. and SUNDMAN, B. Thermodynamic Assessment of the Aluminum Corner of the Al-Fe-Mn-Si System. *Metallurgical and Materials Transactions A*. 2010. Vol. 41, p. 2208–2215.
19. LI, Y. J., ZHANG, W. Z. and MARTHINSEN, K. Precipitation crystallography of plate-shaped Al₆(Mn,Fe) dispersoids in AA5182 alloy. *Acta Materialia*. 2012. Vol. 60, p. 5963–5974.
20. GILLE, P. and BAUER, B. Single crystal growth of Al₁₃Co₄ and Al₁₃Fe₄ from Al-rich solutions by the Czochralski method. *Crystal Research and Technology*. 2008. Vol. 43, p. 1161–1167.
21. KRENDELSBERGER, N., WEITZER, F. and SCHUSTER, J. C. On the constitution of the system Al-Mn-Si. *Metallurgical and Materials Transactions A*. 2002. Vol. 33, p. 3311–3319.
22. CAO, X. a CAMPBELL, J. Morphology of β-Al₅FeSi Phase in Al-Si Cast Alloys. *Materials Transactions*. 2006. Vol. 47, p. 1303–1312.
23. LUO, Z. *A practical guide to transmission electron microscopy: Fundamentals*. New York, NY : Momentum Press, 2016.
24. SMOLA, B. *Transmisní elektronova mikroskopie ve fyzice pevných látek*. Praha : Univerzita Kralova v Praze, 1983.
25. KARLÍK, M. *Úvod do transmisní elektronové mikroskopie*. Praha : České vysoké učení technické v Praze, 2011.
26. KITTEL, Ch. *Introductiotti to Solid State Physics*. John Wiley & Sons, 2004.
27. DE GRAEF, M. *Introduction to conventional transmission electron microscopy*. Cambridge University Press, 2003.
28. GOODHEW, P. J., HUMPHREYS, J. and BEANLAND, R. *Electron Microscopy and Analysis*. London : Taylor & Francis, 2001.
29. BENDERSKY, L. A., GAYLE, F. W. *Electron Diffraction Using Transmission Electron Microscopy*. J Res Natl Inst Stand Technol, 2002.
30. Camera length. *MyScope* [online]. [Accessed 1 May 2019]. Available from: <https://myscope.training/legacy/tem/background/concepts/imagegeneration/diffraction/camerlength/>
31. *DoITPoMS*[online]. [Accessed 2 May 2019]. Available from: <https://www.doitpoms.ac.uk/tlplib/diffraction-patterns/printall.php>

32. LIAO, Y. *Practical electron microscopy and database*. [online]. [Accessed 1 May 2019]. Online book available from: <http://www.globalsino.com/EM/>
33. L.ZHOU, W. and WANG, Z. *Advanced Scanning Microscopy for Nanotechnology*. Beijing : Higher Education Press, 2007.
34. WILKINSON, A. J., BRITTON, B. Strains, planes, and EBSD in materials science. *Materialstoday*. 2012. Vol. 15, p. 366-376.
35. STOJAKOVIC, D. Electron backscatter diffraction in materials characterization. *Processing and Application of Ceramics*. 2012. Vol. 6, p. 1–13.
36. LUKÁŠ, P. *Studium rozdělení disperzních částic v nerovnovážně utužených hliníkových slitinách*. Praha : bakalářská práce, 2009.
37. DUDA, R. O. and HART, P. E. Use of the Hough Transformation to Detect Lines and Curves in Pictures. *Artificial Intelligence Center*. 1971.
38. GRIFFITHS, D. *Introduction to Quantum Mechanics*. Prentice Hall, 1995.
39. Energy Dispersive X-Ray Spectroscopy (EDS). *Energy Dispersive X-Ray Spectroscopy | EDS Failure Analysis | EDS Material Analysis | EDX Failure Analysis | EDX Material Analysis*[online]. [Accessed 28 April 2019]. Available from: <https://www.mee-inc.com/hamm/energy-dispersive-x-ray-spectroscopyeds/>.
40. RAUCH, E. F., PORTILLO, J., NICOLOPOULOS, S., BULTREYS, D., ROUVIMOV, S. and MOECK, P. Automated nanocrystal orientation and phase mapping in the transmission electron microscope on the basis of precession electron diffraction. *Zeitschrift für Kristallographie*. 2010. Vol. 225, p. 103-109.
41. VINCENT, R. and MIDGLEY, P.A. Double conical beam-rocking system for measurement of integrated electron diffraction intensities. *Ultramicroscopy*. 1994. Vol. 53, p. 271–282.
42. ASTAR presentation [online]. [Accessed 28 April 2019]. available on: http://nanocrystallography.research.pdx.edu/media/cms_page_media/15/BerlinASTARII.pdf
43. ROUVIMOV, S., RAUCH, E. F., MOECK, P. and NICOLOPOULOS, S. Automated Crystal Orientation and Phase Mapping of Iron Oxide Nanocrystals in a Transmission Electron Microscope. *Microscopy and Microanalysis*. 2009. Vol. 15, p. 1290–1291.
44. RAUCH, E. F. and VÉRON, M. Automated crystal orientation and phase mapping in TEM. *Materials Characterization*. 2014. Vol. 98, p. 1–9.
45. NISHIKAWA, S. and KIKUCHI, S. Diffraction of Cathode Rays by Mica. *Nature*. 1928. Vol. 121, p. 1019–1020.
46. HUTCHINSON, W.B. Analysis of cellular microstructures in Al–Fe–Si alloy. *Materials Science and Technology*. 2000. Vol. 16, p. 1364–1366.
47. SHAKIBA, M., PARSON, N. and CHEN, X. G. Effect of homogenization treatment and silicon content on the microstructure and hot workability of dilute Al–Fe–Si alloys. *Materials Science and Engineering: A*. 2014. Vol. 619, p. 180–189.

48. BECKER, H. a LEINEWEBER, A. Approximate icosahedral symmetry of α -Al(Fe,Mn,Cr)Si in electron backscatter diffraction analysis of a secondary Al-Si casting alloy. *Materials Characterization*. 2018. Vol. 141, p. 406–411.
49. RAUCH, E. F., VÉRON, M., PORTILLO, J., BULTREYS, D., MANIETTE, Y. and NICOLOPOULOS, S. Automatic Crystal Orientation and Phase Mapping in TEM by Precession Diffraction, *Microscopy and Analysis*. 2008. Issue 93, p. S5–S8.
50. MOECK, P., ROUVIMOV, S., HAUSLER, I., NEUMANN, W. and NICOLOPOULOS, S. Precession electron diffraction & automated crystallite orientation/phase mapping in a transmission electron microscope. *2011 11th IEEE International Conference on Nanotechnology*. 2011.
51. ZHANG, J., HUANG, Y. N., MAO, C. and PENG, P. Structural, elastic and electronic properties of θ (Al₂Cu) and S (Al₂CuMg) strengthening precipitates in Al–Cu–Mg series alloys: First-principles calculations. *Solid State Communications*. 2012. Vol. 152, p. 2100–2104.
52. KTARI, H. H., COUZINIE, J. P., BOURGON, J., CHAMPION, Y. and NJAH, N. Orientation imaging- ASTAR investigation of the grain and precipitate morphology in Al–Cu–Mg alloy processed by Equal Channel Angular Pressing. *Journal of Alloys and Compounds*. 2015. Vol. 647, p. 152–158.
53. GHAMARIAN, I., SAMIMI, P., TELANG, A., VASUDEVAN, V. K. and COLLINS, P. C. Characterization of the near-surface nanocrystalline microstructure of ultrasonically treated Ti-6Al-4V using ASTAR™/precession electron diffraction technique. *Materials Science and Engineering: A*. 2017. Vol. 688, p. 524–531.
54. STADELMANN, P.A. EMS - a software package for electron diffraction analysis and HREM image simulation in materials science. *Ultramicroscopy*. 1987. Vol. 21, p. 131-145.
55. GAO, T., HU, K., WANG, L., ZHANG, B. and LIU, X. Morphological evolution and strengthening behavior of α -Al(Fe,Mn)Si in Al–6Si–2Fe–xMn alloys. *Results in Physics*. 2017. Vol. 7, p. 1051–1054.
56. YAKUBTSOV, I. A., DIAK, B. J., SAGER, C. A., BHATTACHARYA, B., MACDONALD, W. D. and NIEWCZAS, M. Effects of heat treatment on microstructure and tensile deformation of Mg AZ80 alloy at room temperature. *Materials Science and Engineering: A*. 2008. Vol. 496, p. 247–255.
57. Al-Fe-Mn (Aluminium - Iron - Manganese). *Light Metal Systems. Part 2 Landolt-Börnstein - Group IV Physical Chemistry*. p. 1–17.
58. GUSTAFSSON, G., THORVALDSSON, T., DUNLOP, G.L. Metallurgical Transactions A, 1986. Vol. 17A, p. 45-52.
59. NARAYANAN, L. Anantha, SAMUEL, F. H. and GRUZLESKI, J. E. Dissolution of iron intermetallics in Al-Si Alloys through nonequilibrium heat treatment. *Metallurgical and Materials Transactions A*. 1995. Vol. 26, p. 2161–2174.

List of Figures

Figure 1: a) Isothermal section of an Al-Fe-Si ternary phase diagram at 550 °C, b) Al-Fe-Si isothermal section of the Al corner at 500 °C [14].	5
Figure 2: Positive interference of an electron beam scattered on a crystal lattice with interplanar distance of d [25].	7
Figure 3: Ewald construction [23].	9
Figure 4: Formation of high order Laue zones. a) Ewald sphere intersecting several parallel reciprocal lattice planes, b) corresponding diffraction pattern [27].	9
Figure 5: Formation of a Kikuchi lines [28].	10
Figure 6: The intensity of inelastically electron scattering resulting in a formation of a Kikuchi line pattern [28].	10
Figure 7: Formation of Kikuchi lines in a three-dimensional space [24].	11
Figure 8: The difference between a diffraction image observation mode and an image observation mode in TEM [29].	12
Figure 9: a) Camera length, b) effective camera length in TEM.	12
Figure 10: a) Arrangement of sample and electron beam scattering pattern (EBSP) detector with backscatter and forescatter electron detector diodes (BSD) and (FSD) in SEM, b) electron interaction with crystalline material [33].	14
Figure 11: Transformation of Kikuchi lines from a screen into points in a Hough space [36].	14
Figure 12: Parameters of the Hough space [37].	14
Figure 13.: EDS spectrum for TiO ₂ particles on a Cu substrate [33].	15
Figure 14: Scanning direction of the precessing beam over the sample [42].	16
Figure 15: a) Matching of the obtained diffraction patterns and pre-calculated templates represented by red circles. b) Orientation triangle showing the most probable orientation [42].	16
Figure 16: Bright field images of the as cast AA1200 sample.	21
Figure 17: BF image of a dispersoid particle A used for phase identification.	21
Figure 18: Diffractograms obtained from particle A and their corresponding simulated diffractograms of Al ₃ Mn phase with following normal vectors: a) $[1\ 1\ 1]$, b) $[3\ 3\ \bar{1}]$, c) $[\bar{4}\ 0\ 5]$.	22
Figure 19: BF image of a dispersoid particle B used for phase evaluation.	23

Figure 20: Diffractograms obtained from particle B and corresponding simulated patterns of α -Al(Fe,Mn)Si phase with following normal vectors: a) [0 0 1], b) [7 3 1], c) [2 0 3]......24

Figure 21: BF image of the AA1200 sample after annealing at 580° C for 4 hours.25

Figure 22: BF image of dispersoid particles in the annealed AA1200 sample used for the phase determination. The analyzed particle is marked by a circle.26

Figure 23: Diffractograms obtained from TEM and their corresponding simulated patterns of α -Al(Fe,Mn)Si phase with following normal vectors: a) [1 1 1], b) [1 0 2], c) [7 5 1]......27

Figure 24: SEM backscattered electron images of AA1200 alloy annealed at 580 °C for 4 hours.28

Figure 25: EDS analysis of three arbitrarily chosen particles.30

Figure 26: a) EBSD phase evaluation of a dispersoid particle in the aluminum matrix (yellow: Al, green: Al₃Mn, red: α -Al(Fe,Mn)Si), b) inverse pole figure map of the same particle indexed using α -Al(Fe,Mn)Si phase, c) orientation color code map for α -Al(Fe,Mn)Si phase.31

Figure 27: a) EBSD phase evaluation of a dispersoid particle from Fig. 25 without Al₃Mn phase (green: Al, red: α -Al(Fe,Mn)Si), b) inverse pole figure map of the same particle indexed using α -Al(Fe,Mn)Si phase, c) orientation color code map for α -Al(Fe,Mn)Si phase.31

Figure 28: a) EBSD phase evaluation of dispersoids in the aluminum matrix (green: Al, red: α -Al(Fe,Mn)Si), b) EBSD inverse pole image of the same area.32

Figure 29: a) A Kikuchi pattern obtained in one point of the EBSD scan in the dispersoid particle, b) – d) simulated Kikuchi patterns for three most probable orientations of the particle.33

Figure 30: Simulated Kikuchi pattern of a) aluminum, b) α -Al(Fe,Mn)Si, fitted on the aluminum pattern captured in one point of the EBSD scan.33

Figure 31: a) Bright field image of a cluster of particles used for further observations.34

Figure 32: EDS maps of main constituents in dispersoids from Fig. 30.35

Figure 33: a) Inverse pole figure of the annealed sample obtained by ASTAR analysis using a small camera length, b) orientation triangle of a cubic structure.35

Figure 34: A comparison of diffraction patterns and their matched templates for aluminum b), d) and the particle a), c).36

Figure 35: Inverse pole figures of the annealed sample area obtained through ASTAR analysis using larger camera length a) aluminum and α -Al(Fe,Mn)Si particles, b) only α -Al(Fe,Mn)Si particles, c) only aluminum, d) orientation triangle.37

Figure 36: Comparison of apparent bright field (intensity of transmitted primary beam) with an orientation map of the same area.....	37
Figure 37: a)-c) simulated bright field, d)-f) corresponding diffractograms.....	38
Figure 38: Template matching inside one of the particles: a) simulated bright field with a spot in the particle where the diffractogram was taken, b) obtained diffractogram, c) orientation triangle, d) matched template.....	39
Figure 39: Template matching inside one of the particles, a) – d) analogical to the description under Figure 37.....	40
Figure 40: Template matching inside aluminum matrix, a) – d) analogical to the description under Figure 37.....	41
Figure 41: Template matching inside aluminum, a) – d) analogical to the description under Figure 37.....	42
Figure 42: Inverse pole figures with marked lines along which the orientations of [111] zones were calculated a)-c) and plotted in stereographic projections d)-f)....	43

List of Tables

Table 1: Phases found in the ternary Al-Fe-Si and Al-Mn-Si systems and Al-rich corner of Al-Fe-Mn system.....	6
Table 2: The confirmed phases found in the Al-Fe-Mn-Si system with their crystallographic structures and lattice parameters [19-22].....	6
Table 3: Composition of the material AA1200 alloy in wt. %.....	18
Table 4: Composition of main constituents in three particles analyzed by EDS....	29

List of Abbreviations

ASTAR	Automatic Crystal Orientation and phase mapping
EBSD	Electron backscatter diffraction
EDS	Energy-dispersive X-ray spectroscopy
SAED	Selected area electron diffraction
SEM	Scanning electron microscopy
TEM	Transmission electron microscopy
TRC	Twin-roll casting